

THESIS

MICRODOSIMETRIC MEASUREMENTS OF SHIELDING EFFECTS FOR IRON PARTICLES AT 500 MEV/NUCLEON INCIDENT UPON ALUMINUM AND POLYETHYLENE

Submitted by

David R. Farrar

Department of Environmental and Radiological Health Sciences

In partial fulfillment of the requirements

For the Degree of Master of Science

Colorado State University

Fort Collins, Colorado

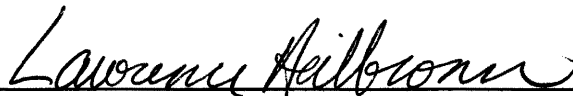
Fall 2007

COLORADO STATE UNIVERSITY

August 23, 2007

WE HEREBY RECOMMEND THAT THE THESIS PREPARED UNDER OUR SUPERVISION BY DAVID R. FARRAR ENTITLED MICRODOSIMETRIC MEASUREMENTS OF SHIELDING EFFECTS FOR IRON PARTICLES AT 500 MEV/NUCLEON INCIDENT UPON ALUMINUM AND POLYETHYLENE BE ACCEPTED AS FULFILLING IN PART REQUIREMENTS FOR THE DEGREE OF MASTER OF SCIENCE.

Committee on Graduate Work



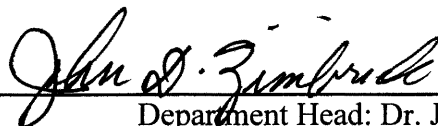
Dr. Lawrence Heilbronn



Dr. Alexander Hulpke



Adviser: Dr. Thomas B. Borak



Department Head: Dr. John Zimbrick

ABSTRACT OF THESIS

MICRODOSIMETRIC MEASUREMENTS OF SHIELDING EFFECTS FOR IRON PARTICLES AT 500 MEV/NUCLEON INCIDENT UPON ALUMINUM AND POLYETHYLENE

The radiation environment in space is very different than on the earth. One portion of the radiation present in space is galactic cosmic radiation (GCR). GCR is composed of protons, alpha particles, and high Z and energy (HZE) particles. One of the most significant HZE particle species in terms of absorbed dose is iron.

One of the dosimetry instruments used on the Space Shuttle and the International Space Station is the tissue equivalent proportional counter (TEPC). It is used to measure absorbed dose and estimate the average quality factor of radiation exposure during manned space missions. TEPCs measure energy deposition in volumes of simulated tissue with dimensions on the order of microns. Spectra of energy depositions are used to calculate values of frequency mean lineal energy, \bar{y}_F , and dose mean lineal energy, \bar{y}_D .

The value of \bar{y}_F can be used to calculate the absorbed dose per particle. Previous studies have found that the choice of \bar{y}_F or \bar{y}_D to approximate particle linear energy transfer (LET), and thus the quality factor, depends on the momentum of the particle and for iron, the value of \bar{y}_D is equivalent. However, the presence of material causes HZE particles to slow down and/or fragment. Thus radiation of one HZE particle species incident on one side of shielding material, insufficient to stop all radiation, will produce a wide range of particles and energies on the other side.

This study exposed a spherical TEPC, in conjunction with a particle spectrometer, to iron particles at 500 MeV/nucleon, produced at the Heavy Ion

Medical Accelerator in Chiba, Japan, with and without shielding material. The shielding material used, in separate measurements, was 1.65 cm Al and 5 cm polyethylene (each has 4.5 g cm^{-2} density thickness). The density thickness is similar to what is used on the Space Shuttle and International Space Station. The absorbed dose per particle was measured and the average LET of the radiation was estimated for each shielding scenario. For iron particles at 500 MeV/nucleon, the shielding did not cause a change in the absorbed dose per particle. But the shielding reduced the average quality factor of the radiation and polyethylene was better than aluminum, at the same density thickness.

David R. Farrar
Department of Environmental and Radiological Health Sciences
Colorado State University
Fort Collins, Colorado 80523
Fall 2007

TABLE OF CONTENTS

ABSTRACT OF THESIS.....	iii
TABLE OF CONTENTS.....	v
LIST OF FIGURES.....	vi
LIST OF TABLES.....	viii
CHAPTER 1 – INTRODUCTION.....	1
CHAPTER 2 – BACKGROUND.....	4
CHAPTER 3 – METHODS & MATERIALS.....	19
CHAPTER 4 – RESULTS & DISCUSSION.....	38
CHAPTER 5 – CONCLUSION.....	56
REFERENCES.....	58

LIST OF FIGURES

Figure 2-1: Relative abundances and absorbed doses from HZE particles in GCR (Simpson 1983).....	6
Figure 3-1: Diagram of TEPC used in the experiment.....	20
Figure 3-2: Diagram of instrumentation apparatus used in measurements with and without shielding material.....	22
Figure 3-3: Diagram of measurement with brass mask.....	24
Figure 3-4: Raw PSD coordinate data (U, V) from measurement with mask.....	25
Figure 3-5: Plot of raw PSD (U_h, V_h), actual (X_h, Y_h), and fitted PSD (X_f, Y_f) coordinates of mask holes.....	26
Figure 3-6: Spectra of energy deposition in the TEPC during the calibration measurements before and after the experiment.....	28
Figure 3-7: Display of the impact parameter of a particle passing through the TEPC.....	29
Figure 3-8: Diagram of δ -rays from a heavy charged particle, traveling through a spherical TEPC, and passing near the gas/wall interface, through the gas cavity, and passing through wall but missing the gas cavity.....	30
Figure 3-9: Corrected PSD coordinates (X_p, Y_p) of events depositing more than 400 keV in TEPC during the measurement without shielding material.....	31
Figure 3-10: Sum of squares (SOS) values of the considered coordinates of the TEPC center (A, B).....	33
Figure 3-11: Distribution of impact parameters of the events that grazed the boundary of the active volume and the wall during the measurement without shielding material.....	34
Figure 4-1: Spectra of energy deposition in the TEPC from events triggered by 10 Hz pulser and 3 mm Si/TEPC coincidence during measurement with no shielding material.....	39
Figure 4-2: Complimentary cumulative distribution probabilities (CCDP) of the spectra shown in Figure 4-1.....	39

Figure 4-3: Calculations of \bar{y}_F and \bar{y}_D with data from measurement without shielding material, over changing cutoff of energy deposition in the TEPC.....	40
Figure 4-4: Spectra of energy deposition in PSDs during measurements with various shielding materials in the iron beamline.....	43
Figure 4-5: Linear calibration of energy deposition in PSD to particle LET.....	44
Figure 4-6: Spectra of energy deposition in the TEPC from particles with low LET and background/noise along with the spectrum of their subtraction, during measurement run with 5 cm polyethylene in beamline.....	46
Figure 4-7: TEPC response functions to all particles emerging from various shielding materials when exposed to iron particles at 500 MeV/nucleon.....	48
Figure 4-8: TEPC response functions to unfragmented iron particle emerging from various shielding materials when exposed to iron particles at 500 MeV/nucleon.....	48
Figure 4-9: TEPC response function from all particles during iron particle irradiation (no shielding material) with the two peaks labeled.....	49
Figure 4-10: Coordinates of events, during measurement with no shielding material, in the first peak ($y \leq 50$ keV/ μm) of the TEPC response function as measured by the PSDs and their distribution of impact parameters.....	50
Figure 4-11: Coordinates of events, during measurement with no shielding material, in the second peak ($100 \leq y \leq 250$ keV/ μm) of the TEPC response function as measured by the PSDs and their distribution of impact parameters.....	50
Figure 4-12: Calculations of \bar{y}_F from measurements with various shielding materials in the beamline.....	52
Figure 4-13: Calculations of \bar{y}_D from measurements with various shielding materials in the beamline.....	52
Figure 4-14: Values of \bar{y}_F , \bar{y}_D , and linear energy transfer (LET) of iron particles at various energies in this experiment and the experiment performed by Gersey et al. (Gersey et al. 2002).....	53

LIST OF TABLES

Table 2-1: Radiation weighting factors for the various types of radiation and energies (ICRP 1991).....	7
Table 2-2: Radiation quality factor (Q) as a function of radiation linear energy transfer (LET) (ICRP 1991).....	8
Table 2-3: Tissue weighting factors. Remainder indicates tissues/organs not listed that can be selectively irradiated and/or are known to be susceptible to cancer induction (ICRP 1991).....	9
Table 2-4: Specific organ dose limits for NASA astronauts (NCRP 2000).....	10
Table 2-5: Ten-year career effective dose limits corresponding to a lifetime excess risk of cancer mortality of three percent (NCRP 2000).....	10
Table 3-1: Ranges of IP the events were sorted into and their respective fractions of the total cross-sectional area of the TEPC.....	37
Table 4-1: Calculated LET and channel # of the peak of energy deposition in the PSDs from unfragmented iron particles during measurements with shielding material in the beam.....	43
Table 4-2: Percentage of events from particles with $LET \leq 10$ keV/ μm measured during the runs with shielding.....	44
Table 4-3: Calculations of \bar{y}_F and \bar{y}_D from measurements of all particles and only unfragmented iron emerging from various shielding materials irradiated with iron particles at 500 MeV/nucleon along with the calculated values of LET of unfragmented iron particles.....	51

CHAPTER 1

Introduction

The radiation environment in space is very different and more damaging than what is found on Earth. It is estimated that astronauts on a three year mission to Mars would receive a dose equivalent of 1 Sv (NCRP 1989) while people living in the US, who receive 3.6 mSv/yr on average (NCRP 1987), would receive an average dose equivalent of 10.8 mSv during the same time frame. Outside the earth's magnetosphere, the largest source of radiation is galactic cosmic radiation (GCR), consisting of particles ranging from protons to high energy and Z (HZE) particles. Iron particles are the most biologically-significant of the HZE particles (NCRP 1989, NCRP 2000).

The Space Shuttle and International Space Station are composed of hulls constructed with aluminum, which gives some radiation protection to the astronaut crews. Polyethylene is used as supplemental radiation shielding and is considered superior to aluminum for shielding HZE particles (Badhwar 2000).

HZE particles traveling through shielding material undergo two types of interactions: slowing down and fragmentation (ICRU 1983). Slowing down is when the particle loses kinetic energy. Fragmentation is when the HZE particle undergoes nuclear collisions, producing secondary particles.

To measure the radiation dose astronauts received during missions in space, NASA employs the use of tissue equivalent proportional counters (TEPCs) on the Space Shuttle and the International Space Station. TEPCs measure discrete energy depositions in simulated volumes of tissue by radiation. Spectra of these energy depositions (TEPC response functions) are used to calculate absorbed dose and estimate the average quality factor of the radiation (Badhwar 1992).

TEPC response functions are used to calculate values of dose mean lineal energy (\bar{y}_D) and frequency mean lineal energy (\bar{y}_F) of the radiation (ICRU 1983). Absorbed dose can be calculated with \bar{y}_F . The average quality factor of radiation is estimated from the average linear energy transfer (LET) of the radiation (ICRP 1991). The LET of the radiation can be approximated with \bar{y}_D or \bar{y}_F . Guetersloh et al. exposed a spherical TEPC to a variety of particle species found in the GCR, each with similar values of LET, and found that the use of \bar{y}_D or \bar{y}_F to approximate the value of LET depended on the momentum of the ion (Guetersloh et al. 2002). Experiments performed by Gersey et al. exposed a spherical TEPC to iron particles, produced at a ground-based accelerator, at energies spanning the GCR spectrum and concluded that \bar{y}_D was a better approximation to the LET of the iron particles than \bar{y}_F (Gersey et al. 2002). However, the experiments with iron particles did not include shielding material and thus did not examine the effect of fragmentation on the response of the TEPC.

In the current experiment, a spherical TEPC was exposed to 500 MeV/nucleon iron particles. The beam of particles was incident on a TEPC and a particle spectrometer that measured the position and LET of particles emerging from the TEPC. Measurements were taken with various shielding materials upstream of the TEPC. The materials used were 1.65 cm of aluminum and 5 cm of polyethylene. These thicknesses of shielding material have the same density thickness of 4.5 g cm^{-2} . Measurements were taken with no shielding material as well. TEPC response functions and values of \bar{y}_F and \bar{y}_D , from a spatially uniform radiation exposure, were calculated from the data collected. This was done for all particles emerging from the shielding material (primary and secondary particles) and for only the iron particles that did not fragment in the shielding material (primary particles). These values were used to determine the effectiveness of the shielding in reducing the equivalent dose from 500 MeV/nucleon iron particles.

CHAPTER 2

Background

Radiation Environment in Space

The radiation present in space is very different from the natural radiation found on the surface of the Earth. On the Earth, natural radiation comes from radionuclides present since the Earth was formed (primordial), radionuclides produced from collisions of space-born atomic nuclei with atoms in the atmosphere and the Earth, and energetic electrons, muons, and neutrons created primarily from the interactions of space-born protons with atoms in the atmosphere (NCRP, 1987). Radiation present in space can be divided into three classifications: trapped particle radiation, solar particle radiation, and galactic cosmic radiation (NCRP, 1989).

Trapped particle radiation consists of electrons and protons spiraling around the geomagnetic field lines and moving between points in the Northern and Southern hemispheres that mirror across the Equator. These trapped particles occur in two concentric zones around the Earth. The “inner” zone extends to about 2.8 Earth radii at the Equator and the “outer” zone spans from 2.8 to 12 Earth radii at the Equator. The energies of the trapped electrons range from 50 keV to 5 MeV and the trapped protons can have energies from 7 MeV to 500 MeV (NCRP, 1989).

Solar particle radiation is radiation emitted from the Sun due to solar flare activity. More specifically, solar particle events occur randomly during the active period of the 11-year solar cycle. The emissions consist of charged particles ranging from protons to helium and heavier nuclei. The energies of these particles can range from a few MeV per nucleon to a few hundred MeV per nucleon, where nucleons refer to the protons and neutrons of the nuclei (NCRP, 1989).

Galactic cosmic radiation (GCR) is omni-directional radiation present throughout the universe and consists of protons, heavy nuclei, electrons, and positrons. The fluence rate is greatest from baryonic particles (atomic particles) with energies from 100 MeV per nucleon to 10 GeV per nucleon. The composition of this GCR subset is 87 percent protons, 12 percent helium nuclei, and one percent heavier nuclei. The heavier nuclei in GCR, often referred to as high Z (atomic number) and energy (HZE) particles, are composed of nuclei of elements ranging in atomic number from lithium to nickel.

Absorbed dose from HZE particles, at similar velocities, is proportional to the product of abundance and Z^2 . Figure 2-1 is a spectrum of the relative abundances of HZE particles in the GCR along with their relative absorbed doses, over the various elements. The top three HZE elements that contribute the largest amounts of relative dose are carbon ($Z = 6$), oxygen ($Z = 8$), and iron ($Z = 26$) (Simpson 1983).

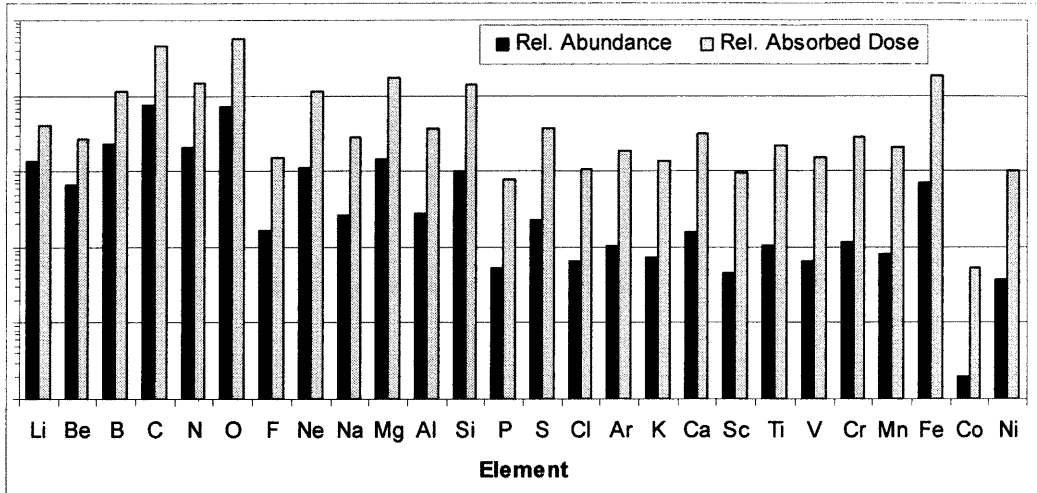


Figure 2-1: Relative abundances and absorbed doses from HZE particles in GCR (Simpson 1983).

Radiation Dosimetry Quantities

The amount of radiation a person receives is regulated in the form of radiation dose limits. The fundamental quantity in radiation dose limits is absorbed dose (D). Absorbed dose is the amount of radiation energy absorbed per unit mass and its unit is the gray (Gy). Absorbed dose is measured for individual tissues or organs (T) and different types and energies of radiation (R), and individual quantities are often stated as $D_{T,R}$ (ICRP 1991).

Absorbed doses are defined for different types and energies of radiation because different types of radiation, incident on identical tissue and at the same absorbed doses, may cause differing amounts of biological damage. To account for these differences, the quantities of radiation weighting factor (w_R) and equivalent dose (H_T) were defined. The radiation weighting factor is a unitless factor that

represents the value of the relative biological effectiveness (RBE) of the type and energy of the radiation (ICRP 1991). Radiation weighting factors are listed in Table 2-1.

Type of Radiation and Energy	Radiation Weighting Factor
Photons, all energies	1
Electrons and Muons, all energies	1
Neutrons, <10 keV	5
Neutrons, 10 keV to 100 keV	10
Neutrons, >100 keV to 2 MeV	20
Neutrons, >2 MeV to 20 MeV	10
Neutrons, >20 MeV	5
Protons, other than recoil protons, >2 MeV	5
Alpha Particles, Fission Fragments, Nonrelativistic Heavy Nuclei	20

Table 2-1: Radiation weighting factors for the various types of radiation and energies (ICRP 1991).

Equivalent dose is a tissue/organ-specific dosimetric quantity, is given in units of sieverts (Sv), and its equation is shown in Equation 2.1 (ICRP 1991).

$$H_T = \sum_R w_R \cdot D_{T,R} \quad \text{Equation 2.1}$$

However, HZE particles are relativistic and do not have a defined radiation weighting factor. The ICRP defined a method for calculating equivalent dose from radiation without a radiation weighting factor by using the radiation quality factor (Q) of the radiation (ICRP 1991). The radiation quality factor of HZE particles can be calculated from their linear energy transfer (LET), energy lost by collisions per unit track length through the medium, as shown in Table 2-2.

<i>LET</i> (keV μm^{-1})	<i>Q</i>
< 10	1
10 - 100	$0.32 \text{ LET}^{-2.2}$
> 100	$300 \text{ LET}^{-0.5}$

Table 2-2: Radiation quality factor (*Q*) as a function of radiation linear energy transfer (*LET*) (ICRP 1991).

Using absorbed dose and the radiation quality factor (both *LET* dependent), the equivalent dose can be calculated as shown in Equation 2-2 (ICRP 1991).

$$H_T = \int_{LET} Q \cdot D_T \cdot dLET \quad \text{Equation 2-2}$$

In addition to the differences in biological effectiveness due to energy and type of radiation, tissues and organs do not respond to radiation equally. Specifically, tissues and organs have different probabilities of stochastic effects when exposed to the same equivalent dose. Two additional values were defined: tissue weighting factor (w_T) and effective dose (*E*). Tissue weighting factors represent the relative contributions, from the tissues and organs, to the total detriment due to uniform whole body irradiation (ICRP 1991). Table 2-3 lists the tissue weighting factors.

Tissue or Organ	Tissue Weighting Factor
Gonads	0.20
Red Bone Marrow	0.12
Colon	0.12
Lung	0.12
Stomach	0.12
Bladder	0.05
Breast	0.05
Liver	0.05
Esophagus	0.05
Thyroid	0.05
Skin	0.01
Bone Surface	0.01
Remainder	0.05

Table 2-3: Tissue weighting factors. Remainder indicates tissues/organs not listed that can be selectively irradiated and/or are known to be susceptible to cancer induction (ICRP 1991).

Effective dose is a dosimetric quantity that is a summation, over all irradiated tissues and organs, of the products of tissue/organ specific equivalent doses with their associated tissue weighting factors, as shown in Equation 2.2 (ICRP 1991).

$$E = \sum_T w_T \cdot H_T$$

Equation 2-2

The National Aeronautics and Space Administration's (NASA) radiation dose limits for astronauts in manned space missions are defined for bone marrow, eye, and skin. There are also limits on effective dose (NCRP 2000).

NASA's radiation dose limits for specific organs are defined in units called gray-equivalents (Gy-Eq). The gray-equivalent is defined as the product of the

absorbed dose to the organ, in gray, and the value of the relative biological effectiveness of the radiation. These limits are designed to prevent the late deterministic effects from occurring in the particular organs of the astronauts due to radiation exposure, and are shown in Table 2-4 (NCRP 2000).

	Bone Marrow (Gy-Eq)	Lens of the Eye (Gy-Eq)	Skin (Gy-Eq)
Career	-	4.0	6.0
1 year	0.50	2.0	3.0
30 days	0.25	1.0	1.5

Table 2-4: Specific organ dose limits for NASA astronauts (NCRP 2000).

The other portion of NASA’s radiation exposure limits for astronauts are based on the total effective doses accrued during manned space missions. The quantities of these limits are designed to limit the excess lifetime risk of developing fatal cancer from the radiation exposure to three percent. These limits are a function of age of first exposure and gender of the astronauts (NCRP 2000). Table 2-5 shows ten-year career effective doses for astronauts at various ages of first exposure.

Age at First Exposure (years)	Female Effective Dose Limit (Sv)	Male Effective Dose Limit (Sv)
25	0.4	0.7
35	0.6	1.0
45	0.9	1.5
55	1.7	3.0

Table 2-5: Ten-year career effective dose limits corresponding to a lifetime excess risk of cancer mortality of three percent (NCRP 2000).

NASA has used various types of onboard radiation detection devices to measure radiation levels during manned space missions in order to determine the

radiation dose to the astronauts. These devices can be classified as either passive or active dosimeters.

Passive dosimeters are devices that utilize radiation sensitive materials that store information about the radiation exposure. The information is integrated over the exposure time and can be read only after the radiation exposures. Therefore, these devices can only be used to determine total amount of radiation dose or time-weighted average dose rate. These devices do not require a power supply or electronics to record the dosimetric information and thus tend to be small and robust. Some examples of such devices used by NASA are plastic track detectors, neutron activation foils, and thermo luminescent dosimeters (TLD) (NCRP 2000).

Active dosimeters, on the other hand, give radiation exposure data as it occurs. These devices can be used to measure and report dynamic dose rates as well as integrated doses. Active dosimeters require power supplies, signal electronics, and sometimes computers in order to store, calculate, and report the real-time radiation measurements. One type of active dosimeter that NASA uses during manned space missions is the tissue equivalent proportional counter (NCRP 2000, Badhwar et al. 1992).

Tissue Equivalent Proportional Counter

Tissue equivalent proportional counters (TEPC) are active radiation dosimeters used during manned space missions that measure the absorbed dose and equivalent dose (as well as the rates of each of these quantities) of the space radiation environment. The detectors are composed of a cavity containing low-pressure tissue equivalent gas and an anode wire assembly, both surrounded by a tissue equivalent plastic wall. They are designed to measure radiation dosimetry of simulated tissue with size similar to single mammalian cells (microdosimetry). The plastic wall and gas are tissue equivalent in that they have elemental compositions similar to biological tissue. These detectors measure energy deposition events of the radiation passing through the gas cavity. The events can be compiled into frequency distribution spectra (often called TEPC response functions) and these spectra can be used to ascertain estimates of the average linear energy transfer (\overline{LET}) of the radiation field, which can be used to determine the average quality factor (\overline{Q}) (Knoll 2000) and calculate equivalent dose.

Interactions of HZE Particles in Matter

HZE particles (projectiles) interact with atoms in matter (target atoms) in two ways: Coulomb interactions and nuclear collisions. Coulomb interactions occur when the positive charge of the projectile reacts with the negative charge of the electrons orbiting the target atom. This ionizes the target atom and reduces the energy of the projectile (ICRU 1983). This energy reduction causes the projectile to slow down and

increase its stopping power (energy loss over distance traveled in the medium)

$\left(-\frac{dE}{dx}\right)$ as shown by Equation 2-3,

$$-\frac{dE}{dx} = \frac{4\pi k_0^2 z^2 e^4 n}{mc^2 \beta^2} \left[\ln \frac{2mc^2 \beta^2}{I(1-\beta^2)} - \beta^2 \right] \quad \text{Equation 2-3}$$

where k_0 is $8.99 * 10^9 \text{ N m}^2 \text{ C}^{-2}$, z is the atomic number of the projectile, e is the charge of an electron, n is the number density of electrons in the medium, m is the rest mass of the electron, c is the speed of light in vacuum, β is the speed of the projectile relative to c , and I is the mean excitation energy of the medium (Turner 1995). Because of the increase in the stopping power of the projectile, HZE particles that undergo Coulomb interactions in the medium will deposit more energy than before, increasing the absorbed dose.

However, HZE particles can also have nuclear collisions in media. Nuclear collisions can cause the projectile to fragment, producing particles of smaller atomic numbers. The fragments have velocities approximately equal to the parent projectile. The stopping power of HZE particles, as shown in Equation 2-3, is proportional to the atomic number of the particle squared. All particles produced by fragmentation will deposit less energy than the parent particle. Therefore, the absorbed dose will decrease.

Microdosimetry Quantities

The energy deposited in the TEPC by a single energy-deposition event is called the energy imparted (ε) (ICRU 1983). The events can be used to produce a probability density function of energy imparted in the TEPC ($f(\varepsilon)$).

The average path length of random straight lines passing through a simulated convex cavity, assuming the condition of mean free path randomness or μ -randomness (Kellerer et al. 1968), is called the mean chord length ($\bar{\ell}$). Lineal energy (y) is defined as the quotient of the energy imparted by the mean chord length, as shown in Equation 2-4 (ICRU 1983).

$$y = \frac{\varepsilon}{\bar{\ell}} \qquad \text{Equation 2-4}$$

The units of lineal energy are often given in keV μm^{-1} . The equation for mean chord length is shown in Equation 2-5,

$$\bar{\ell} = \frac{4V}{S} \qquad \text{Equation 2-5}$$

where V is the volume of the cavity and S is the surface area. For a spherical cavity, $\bar{\ell}$ is two-thirds the diameter.

The probability density function of the spectrum of lineal energy, $f(y)$, is used to calculate the frequency-mean lineal energy (\bar{y}_F) and the dose-mean lineal energy (\bar{y}_D) as shown in Equations 2-6 and 2-7 (ICRU 1983):

$$\bar{y}_F = \int_0^{\infty} y f(y) dy \quad \text{Equation 2-6}$$

$$\bar{y}_D = \frac{1}{\bar{y}_F} \int_0^{\infty} y^2 f(y) dy \quad \text{Equation 2-7}$$

Since the measurements from TEPCs yield spectra of ε and the TEPC used in the experiment is spherical, Equations 2-6 and 2-7 can be rewritten as shown below (Gersey 2006),

$$\bar{y}_F = \frac{\sum \varepsilon \cdot N(\varepsilon) d\varepsilon}{\frac{2}{3} D_c} \quad \text{Equation 2-8}$$

$$\bar{y}_D = \frac{\sum \varepsilon^2 \cdot N(\varepsilon) d\varepsilon}{\left(\frac{2}{3} D_c\right)^2 \cdot \bar{y}_F} \quad \text{Equation 2-9}$$

where $N(\varepsilon)d\varepsilon$ is the probability distribution function of ε and D_c is the diameter of the active volume of the spherical TEPC.

The value of \bar{y}_F can be used to calculate the absorbed dose from HZE particles as shown in Equation 2-10,

$$\text{Absorbed Dose} = \frac{3N_{\text{particles}} \cdot \bar{y}_F \cdot D_c}{2\rho_g \cdot V_g} \quad \text{Equation 2-10}$$

where $N_{\text{particles}}$ is the number of HZE particles, ρ_g is the density of the gas in the TEPC, and V_g is the volume of the gas in the TEPC (Gersey 2006).

Previous Work

A number of studies have been conducted in order to characterize the TEPC response functions to various HZE particles at various energies of the GCR spectrum. Rademacher et al. examined the response of a spherical TEPC (simulating 1, 2, and 3 μm diameter tissue) when exposed to a beam of 1 GeV/nucleon ^{56}Fe ions. They looked at the effects of the plastic wall/gas cavity interface on the response of the detector and determined that the effective wall thickness required to achieve charged-particle equilibrium is 2.54 mm (Rademacher et al. 1998). Guetersloh et al. exposed a spherical TEPC to four heavy ions (^{14}N , ^{16}O , ^{20}Ne , and ^{28}Si) with the same LET (about 43 keV/ μm) and the work indicated that the choice of using \bar{y}_F or \bar{y}_D to determine the average radiation quality factor and absorbed dose depends on the momentum of the ion (Guetersloh et al. 2002). Taddei et al. analyzed the response of a spherical TEPC to various ions (^4He , ^{12}C , ^{16}O , ^{28}Si , and ^{56}Fe) at similar velocities.

For incident particles with LET greater than $10 \text{ keV } \mu\text{m}^{-1}$, they found that the value of \bar{y}_F was always less than the LET and the value of \bar{y}_D was approximately equal to the LET (Taddei et al. 2006). Gersey et al. exposed a spherical TEPC to ^{56}Fe energies from 200-1000 MeV/nucleon, compiled TEPC lineal energy spectra and the values of \bar{y}_F and \bar{y}_D of the various iron energies (Gersey et al. 2002). They determined that charged particle equilibrium was achieved for each of the iron energies examined, allowing for the calculation of absorbed dose from these particles to be proportional to the LET and fluence of the particles.

Wilson et al. discussed shielding of HZE particles. They stated that shielding materials with low atomic number, when exposed to HZE particles, produce a range of low LET particles that are less biologically damaging in relation to the HZE particles (Wilson et al. 1995).

Contributions From This Work

The purpose of this work was to examine the effects of shielding material on a species of HZE particles with a TEPC, a type of microdosimeter. A spherical TEPC, along with a particle spectrometer, was exposed to a beam of iron particles with energy of 500 MeV/nucleon. This particle type and energy is a part of the GCR and gives considerable radiation dose to astronauts during manned space missions. TEPC response functions were measured with 1.65 cm-thick aluminum, 5 cm-thick polyethylene, and no material shielding the TEPC. Aluminum is used to construct

spacecraft hulls. In comparison to aluminum, polyethylene is considered a superior GCR shielding material (Badhwar et al. 2000). Aluminum with a thickness of 1.65 cm and polyethylene with a thickness of 5 cm have a density thickness of 4.5 g cm^{-2} . This density thickness is within 10 % of the typical density thickness of material surrounding the human-occupied area of a space vehicle (5 g cm^{-2}) (Wilson et al. 1999). Density thickness of a quantity of material is the product of the density and thickness.

TEPC response functions of each shielding scenario, from uniform irradiation of iron particles, were compiled from the data collected. Response functions were constructed from all of the particles emerging from the shielding materials (primary and secondary particles) and from only the unfragmented iron particles (primary particles) emerging from the shielding material. Those response functions were then used to calculate values of \bar{y}_F and \bar{y}_D . These quantities were used to evaluate the effectiveness of aluminum and polyethylene, with equivalent density thickness, in reducing the equivalent dose from 500 MeV/nucleon iron particles.

CHAPTER 3

Methods & Materials

The experiment was designed to measure the effects of shielding on iron particles at 500 MeV/nucleon ($\beta = 0.76$) with a tissue equivalent proportional counter (TEPC). The shielding materials, used in separate measurements, were 1.65 cm-thick aluminum (4.5 g cm^{-2}) and 5 cm-thick polyethylene (4.5 g cm^{-2}). The TEPC was also exposed to iron particles with no shielding material. The beam of iron particles was generated at the Heavy Ion Medical Accelerator (HIMAC) located at the National Institute of Radiological Sciences (NIRS) in Chiba, Japan.

The HIMAC is the first heavy ion accelerator dedicated to medicine in the world (NIRS 1992). The facility is capable of accelerating ions, ranging from protons to iron nuclei, to energies ranging from 100 to over 1000 MeV/nucleon. Not only does this ion acceleration capability allow for treatment of deep-seated and radiation-resistant tumors (NIRS 1992), these ions and energies are also apart of the GCR spectrum. Therefore, experiments involving the GCR spectrum can be conducted at this ground-based facility.

The TEPC used in the experiment was spherical and had a $\frac{1}{2}$ " (12.7 mm) active volume diameter, as shown in Figure 3-1.

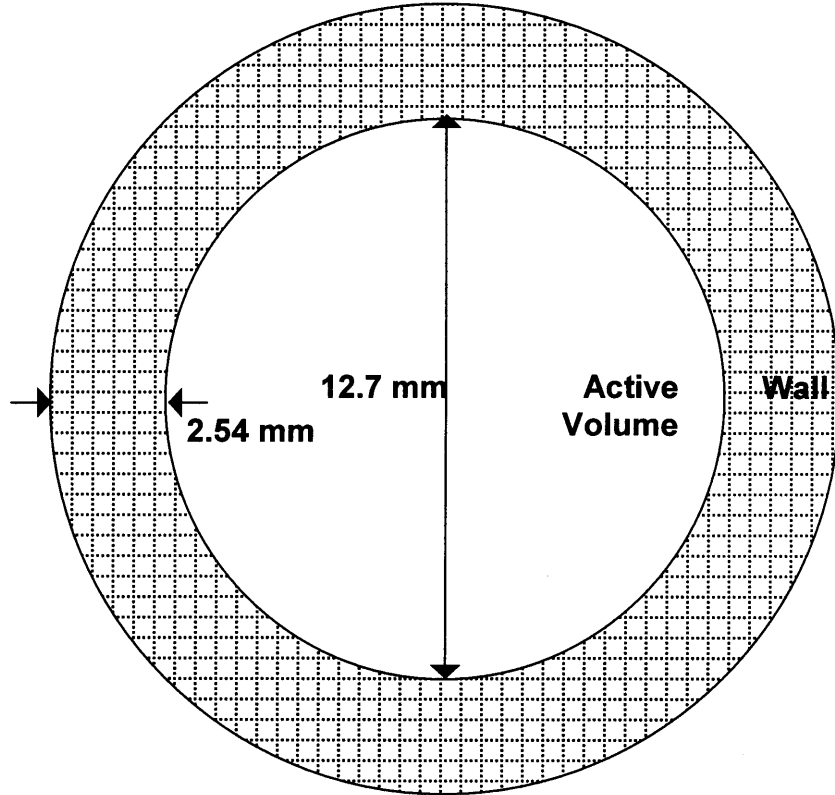


Figure 3-1: Diagram of TEPC used in the experiment.

In order for an instrument to simulate a volume of tissue for dosimetry purposes, the energy deposition (ΔE) in the active volume of the instrument (av) and in the simulated tissue (t) by identical radiation must be the same as shown in Equation 3-1,

$$\Delta E_t = (S/\rho)_t \rho_t d_t = (S/\rho)_{av} \rho_{av} d_{av} = \Delta E_{av} \quad \text{Equation 3-1}$$

where (S/ρ) is the mass stopping power, ρ is the density, and d is the diameter (ICRU 1983).

The active volume of the TEPC consists of gas with a similar elemental composition as tissue. Thus the mass stopping power of the active volume is the same for tissue. After simplifying Equation 3-1, a relation between the properties of the active volume and the tissue being simulated is shown in Equation 3-2.

$$\rho_t d_t = \rho_{av} d_{av} \qquad \text{Equation 3-2}$$

Using this relation, the pressure of the tissue equivalent gas in the 12.7 mm-wide active volume of the TEPC must be 33 Torr in order to simulate a spherical volume of tissue with a diameter of 1 μm . Therefore, the TEPC was filled with tissue equivalent gas at that pressure prior to the experiment.

The instrument setup used during the measurements with and without shielding material is shown in Figure 3-2.

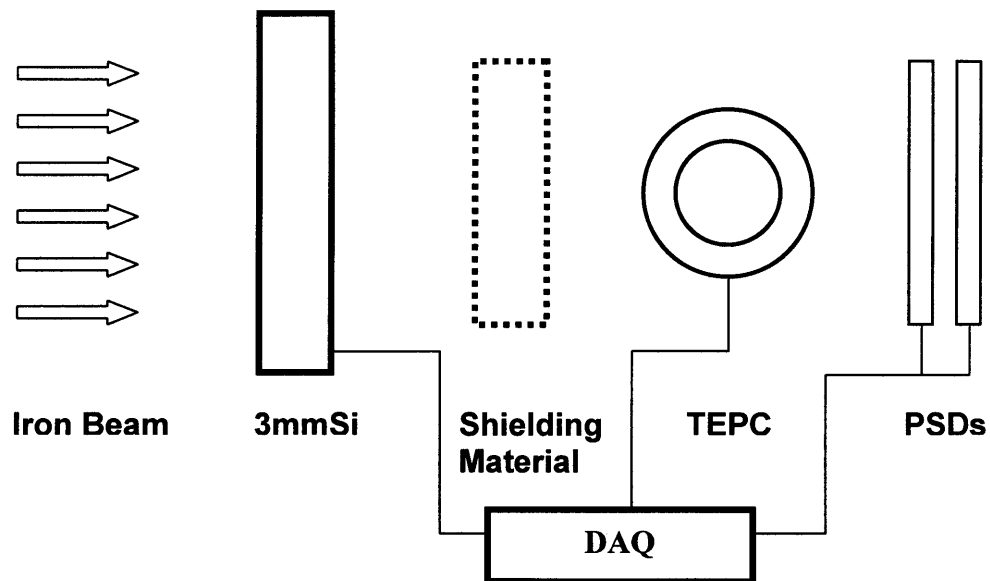


Figure 3-2: Diagram of instrumentation apparatus used in measurements with and without shielding material.

The iron particles were incident on a series of detectors and shielding material (if any). First in line was a 3 mm-thick silicon detector (3mmSi). This detector measured how much energy was deposited by particles incident on itself. Not only did the response from this detector indicate that a particle was traversing the instrumentation apparatus, but it allowed for the determination of whether that particle was iron or a fragment. Next along the beamline was the shielding material used in the run (if any). After that was the TEPC. The final instruments downstream in the beam line were a pair of positional silicon detectors (PSDs). Each PSD measured the energy deposition of particles incident upon itself as well as their positional coordinate in the plane perpendicular to the beam line. The PSDs were placed as close to the TEPC as possible and were oriented so they could determine if and where particles emerged from the TEPC. The trigger the DAQ used to record an

event was the coincidence of the signal from the 3mmSi and the TEPC (both above a set threshold).

The DAQ recorded the signals from the 3mmSi, TEPC and PSDs (after they were amplified and processed) each time the conditions for a trigger were met (Taddei 2003). The data was stored event-by-event and analyzed offline with Physics Applied Workshop (PAW). All analyses, involving the measurements with the iron beam, stated in this thesis were begun by selecting events that the 3 mm Si detector measured as an unfragmented iron particle and discarding the remainder (unless stated otherwise). Since these analyses were performed with events that the 3 mm Si detector measured to be unfragmented iron particles, the fragmentation of iron measured was due to the shielding material, TEPC, and/or PSDs only.

Calibration of PSD Positional Data

The PSDs measure energy deposited by particles incident on themselves as well as their locations in the plane perpendicular to the particle beam. The positional measurements made by the PSDs (U , V) are orthogonal to one another, but require calibration in order to yield accurate coordinates of the particles (X_p , Y_p). To do this, a measurement run was taken with the iron beam incident on the 3 mm-thick silicon detector, a brass “mask”, and the PSDs, as shown in Figure 3-3.

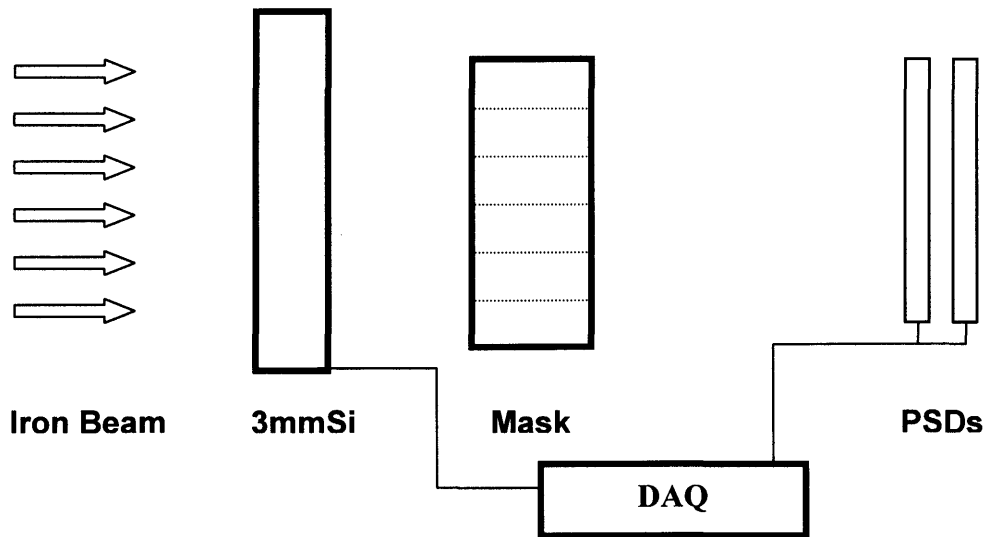


Figure 3-3: Diagram of measurement with brass mask.

The mask is a 2.54 cm thick slab of brass with 0.8 mm wide holes drilled in it. The holes are in a radial pattern, emanating from the center and in 6.35 mm intervals. The mask was designed so that iron particles incident on it do not penetrate except when they travel through the holes. Figure 3-4 shows the raw coordinate data from the PSDs (U, V) collected during the measurement run with the mask.

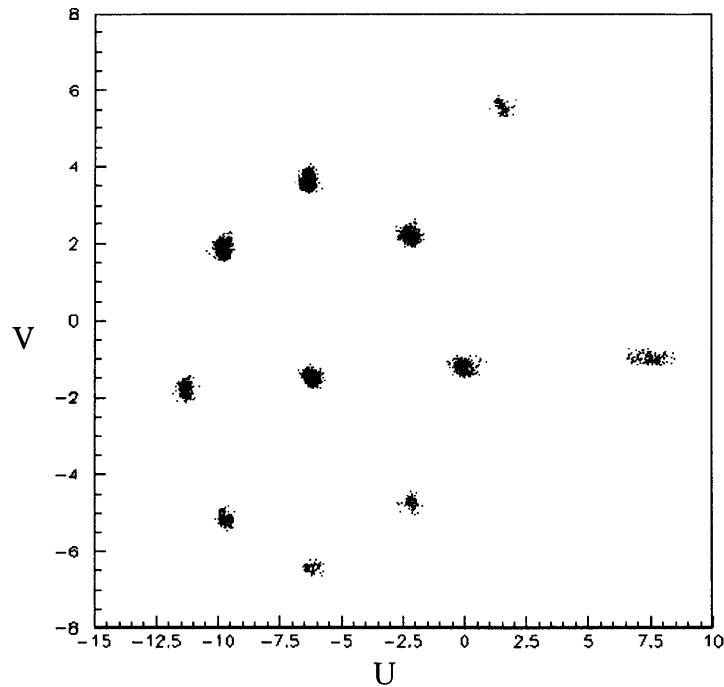


Figure 3-4: Raw PSD coordinate data (U, V) from measurement with mask.

Only 11 of the holes in the mask showed up in the raw PSD coordinate data due to the sagging of the mask mount during the measurement, the lack of uniformity of the beam, and possible divergence/convergence of the beam. The coordinates of the centers of the holes in the raw PSD data were found by selecting the points corresponding to a hole, fitting Gaussian distributions to the distributions of U and V of those points, and repeating the process for each of the other holes. Because the holes in the mask were drilled in a known pattern, the centers of the holes, in the view of the PSDs (U_h, V_h), were fitted to their actual locations (X_h, Y_h), as shown in Equations 3-3 and 3-4

$$X_h = A + B * U_h + C * V_h + D * U_h^2 + E * V_h^2 \quad \text{Equation 3-3}$$

$$Y_h = F + G * U_h + H * V_h + J * U_h^2 + K * V_h^2$$

Equation 3-4

where $A-K$ are constants.

Figure 3-5 displays a plot of the fitted PSD coordinates of the holes (X_f, Y_f) with their actual locations (the center mask hole being the origin) and their raw PSD coordinates.

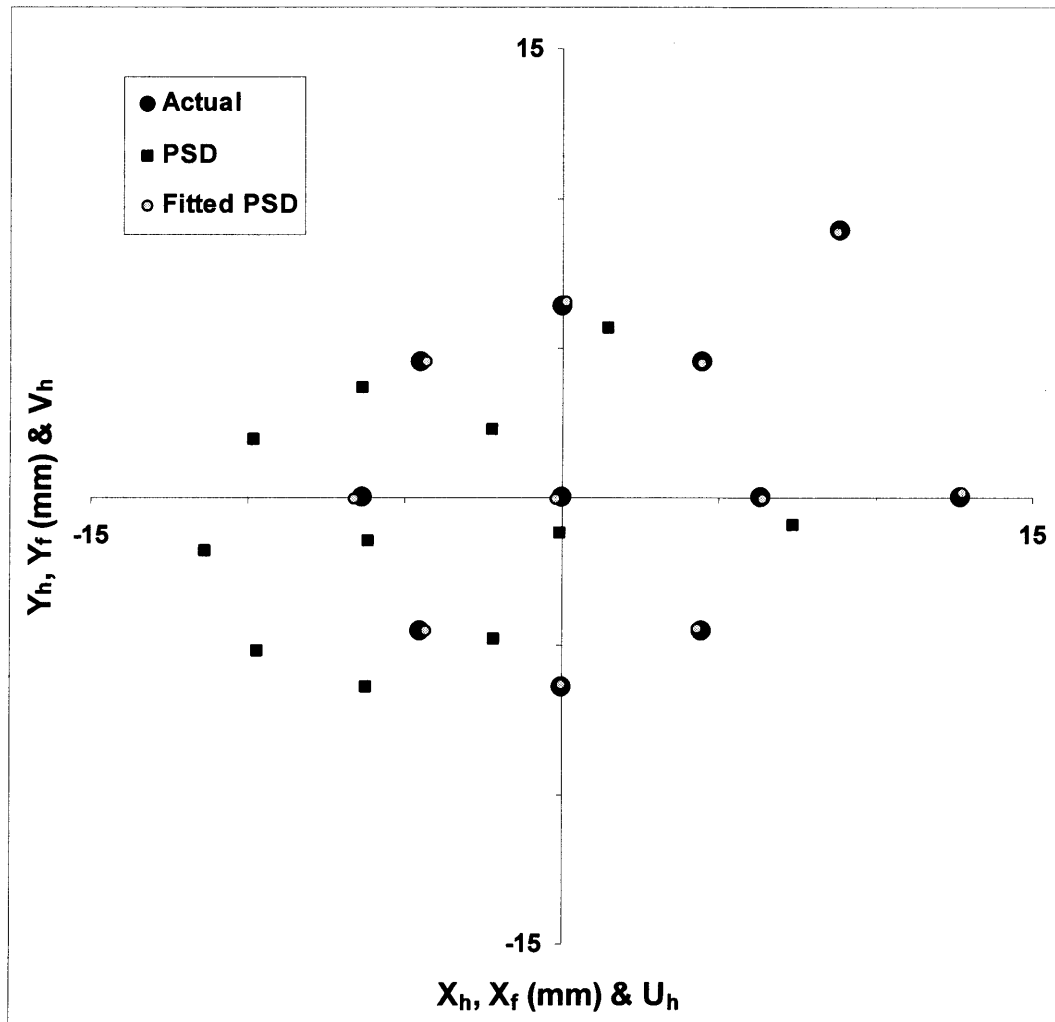


Figure 3-5: Plot of raw PSD (U_h, V_h), actual (X_h, Y_h), and fitted PSD (X_f, Y_f) coordinates of mask holes.

The mean difference in distance between the actual coordinates and the fitted PSD coordinates is 0.134 mm with a standard deviation of 0.078 mm. Equations 3-3 and 3-4, using the constants derived from the fit of the holes, were applied to all raw positional measurements made by the PSDs (U, V) to yield corrected coordinates (X_p , Y_p) of the particles. However, the sagging of the mask in relation to the TEPC caused the origin of the corrected coordinates to not correlate to the center of the TEPC. Therefore, all of the corrected coordinates of the particles need to be translated in order for the origin to correspond to the center of the TEPC. This is addressed later on in this chapter in the section entitled *Impact Parameter*.

Energy Calibration of TEPC

Before and after the experiment, energy calibration measurements of the TEPC were performed. This was done by exposing the active volume to an internally mounted $<1 \mu\text{Ci } ^{244}\text{Cm } \alpha\text{-particle}$ source and taking measurements of the energy deposition with the TEPC. Because the iron beam was not present during these measurements, the recording of data by the DAQ was initiated by the TEPC only. The spectra of energy deposition in the TEPC during the calibration measurements before and after the experiment are displayed in Figure 3-6.

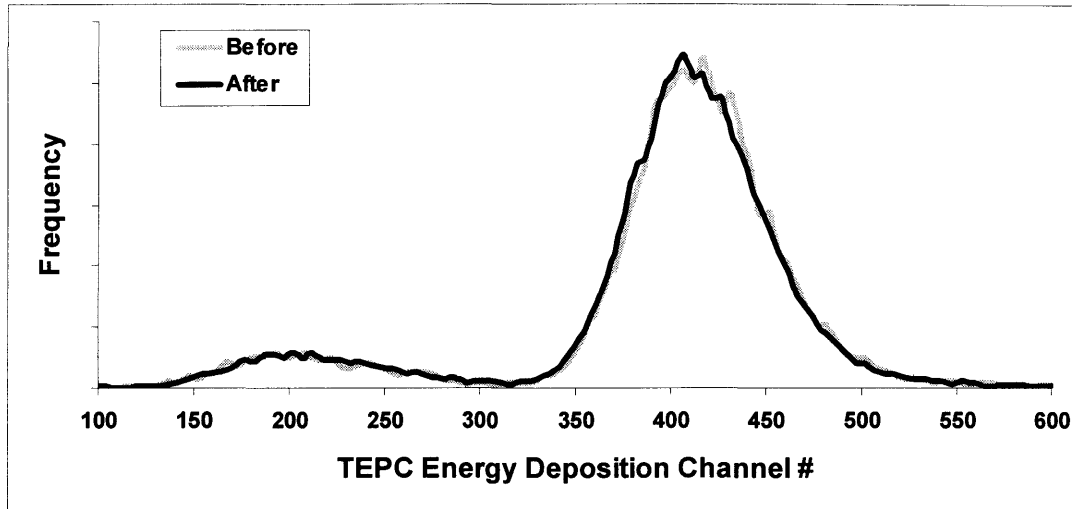


Figure 3-6: Spectra of energy deposition in the TEPC during the calibration measurements before and after experiment.

The large peak of each TEPC calibration spectra was fit to a Gaussian distribution. ^{244}Cm is effectively a monoenergetic alpha emitter and the peak corresponds to the alpha particles from the internal source traversing the diameter of the active volume, depositing 84.15 keV in the process (Taddei 2004).

Another known amount of energy deposition in the TEPC, correlated to a channel # of energy deposition in the TEPC, is zero energy deposited in the TEPC. This channel # was determined by finding the lowest channel # of energy deposition in the TEPC at which events were recorded. Using this channel # to be zero energy deposited in the TEPC and the previously found channel # corresponding to 84.15 keV, a linear calibration of the energy deposition in the TEPC data was created and used in the offline analysis.

Impact Parameter

The amount of energy deposited in the TEPC by individual heavy charged particles depends not only on the particle charge and energy but also on the path through the TEPC. The path length of a particle through the active volume of the TEPC is related to the impact parameter or distance of closest approach to the center of the TEPC, as shown in Figure 3-7.

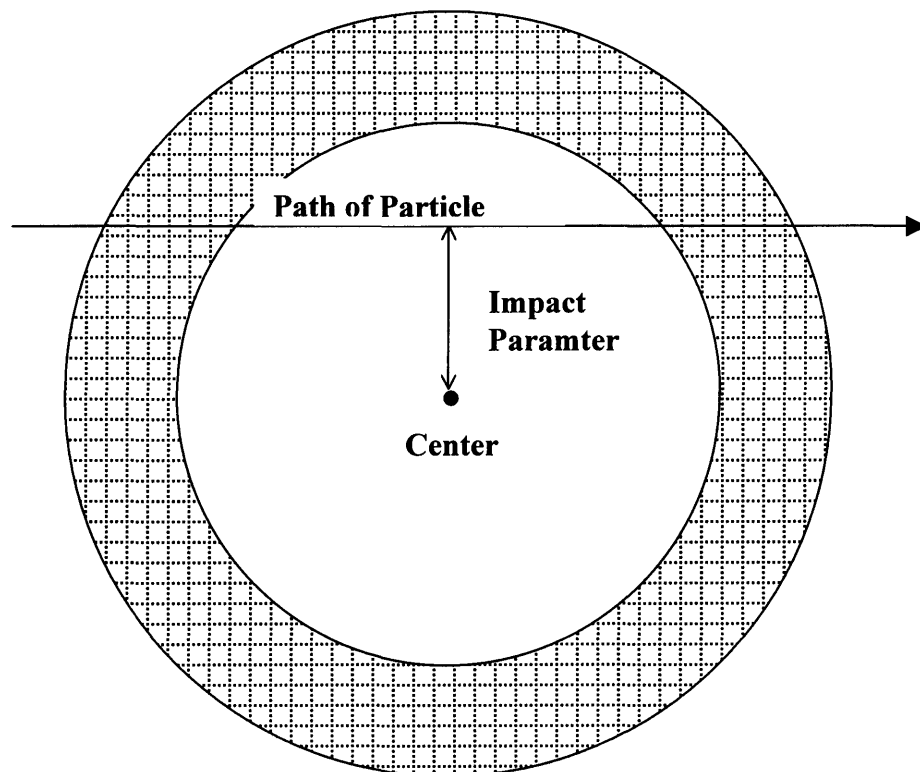


Figure 3-7: Display of the impact parameter of a particle passing through the TEPC.

Heavy charged particles passing near the wall/gas interface of the TEPC generate a large number of δ -rays (liberated electrons) that reach the active volume. These collections of δ -rays register as events with large energy deposition by the TEPC. Likewise, particles traveling through the gas cavity create a smaller number of δ -rays in the gas cavity, registering as events with smaller energy depositions. Also, particles that pass through the wall but miss the gas cavity produce an even smaller number of δ -rays that reach the cavity, producing a relatively small measurement by the TEPC. A diagram of these three types of interactions in the TEPC is shown in Figure 3-8.

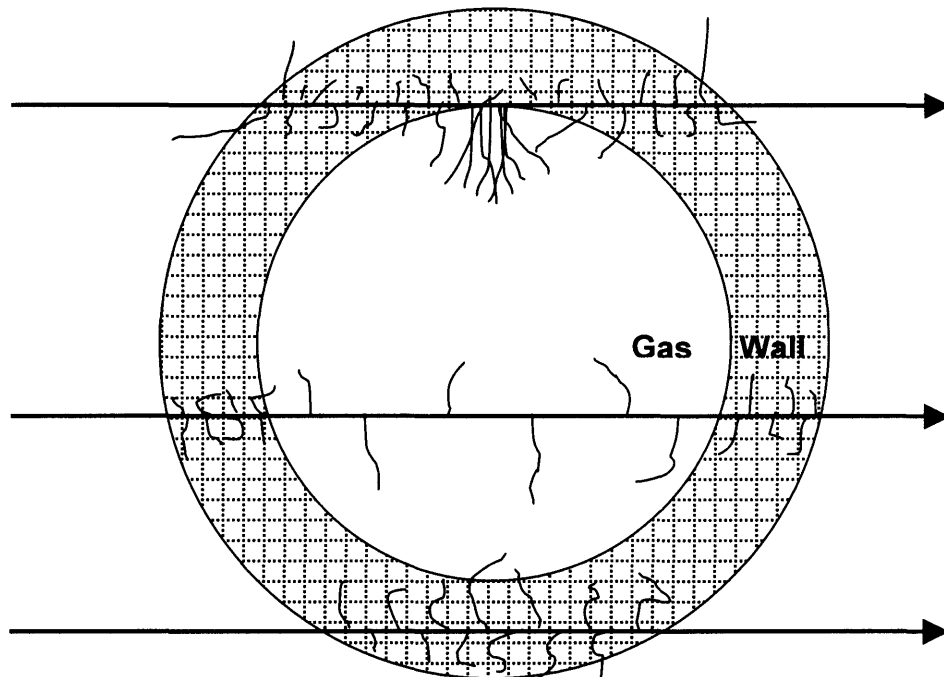


Figure 3-8: Diagram of δ -rays from a heavy charged particle, traveling through a spherical TEPC, and passing near the gas/wall interface, through the gas cavity, and passing through wall but missing the gas cavity.

In order to calculate the impact parameters of the events, the center of the TEPC had to be located in the corrected PSD coordinate system (X_p , Y_p). This was done by examining events that traveled near the wall/cavity boundary of the TEPC. These events were selected in the data from the measurement run with no shielding material. This was done by choosing events that deposited more than 400 keV in the TEPC. Figure 3-9 displays the corrected coordinates (X_p , Y_p) of these events.

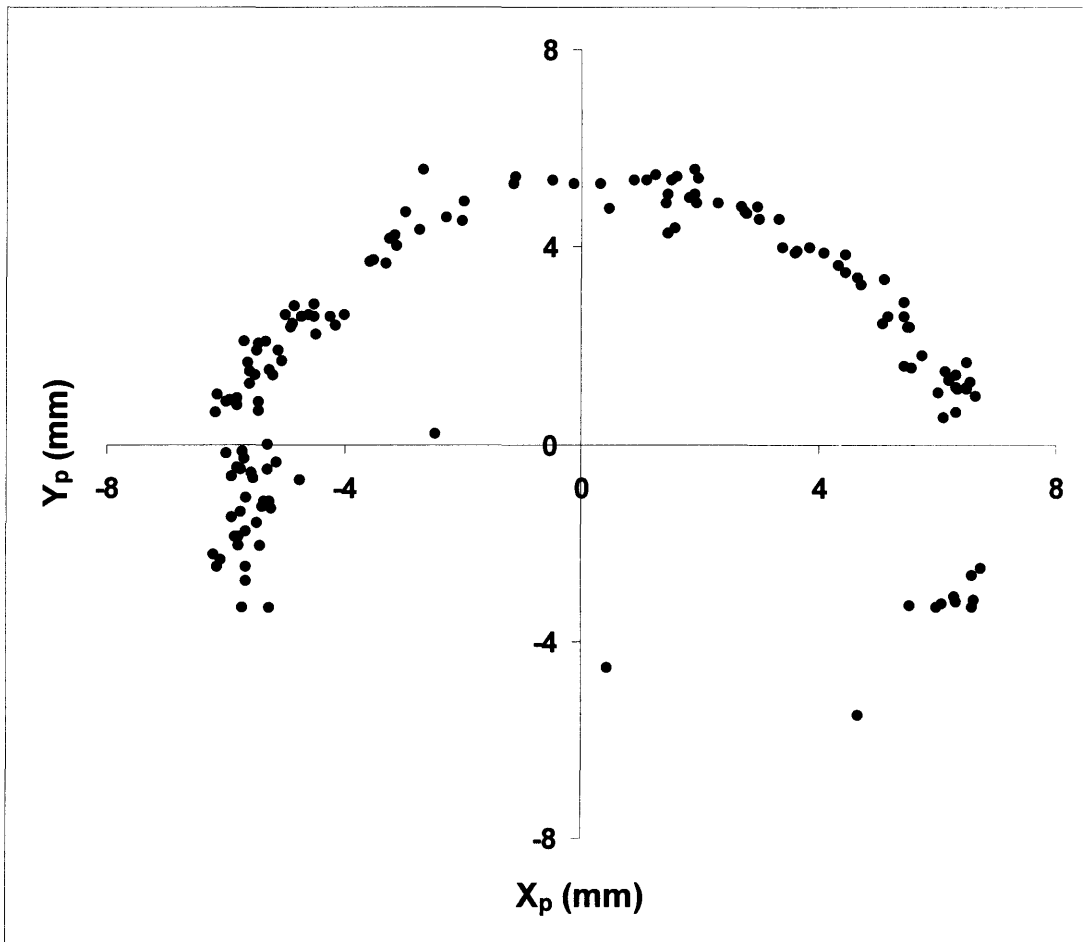


Figure 3-9: Corrected PSD coordinates (X_p , Y_p) of events depositing more than 400 keV in TEPC during the measurement without shielding material.

The bottom portion of the TEPC wall/cavity boundary does not show in the figure due to the lack of spatial uniformity of the iron beam. Nevertheless, the center of these “grazer” events was located by performing a least squares analysis. The analysis calculated how far away each event was from the perimeter of a circle with a radius of 6.35 mm (active volume of TEPC) centered on a test TEPC center coordinate (A, B). These differences in distance were squared and then added together, yielding a sum-of-squares (SOS) value indicating how well the circle, centered on (A, B), fit the events. Equation 3-3 shows how the sum-of-squares values were calculated

$$SOS = \sum_{grazer} \left(\sqrt{(X_{grazer} - A)^2 + (Y_{grazer} - B)^2} - 6.35 \text{ mm} \right)^2 \quad \text{Equation 3-5}$$

where X_{grazer} & Y_{grazer} are the corrected PSD coordinates of an event that deposited over 400 keV in the TEPC.

A computer program stepped through values of A and B and calculated an SOS value for each of them. Figure 3-10 displays a contour plot of the results.

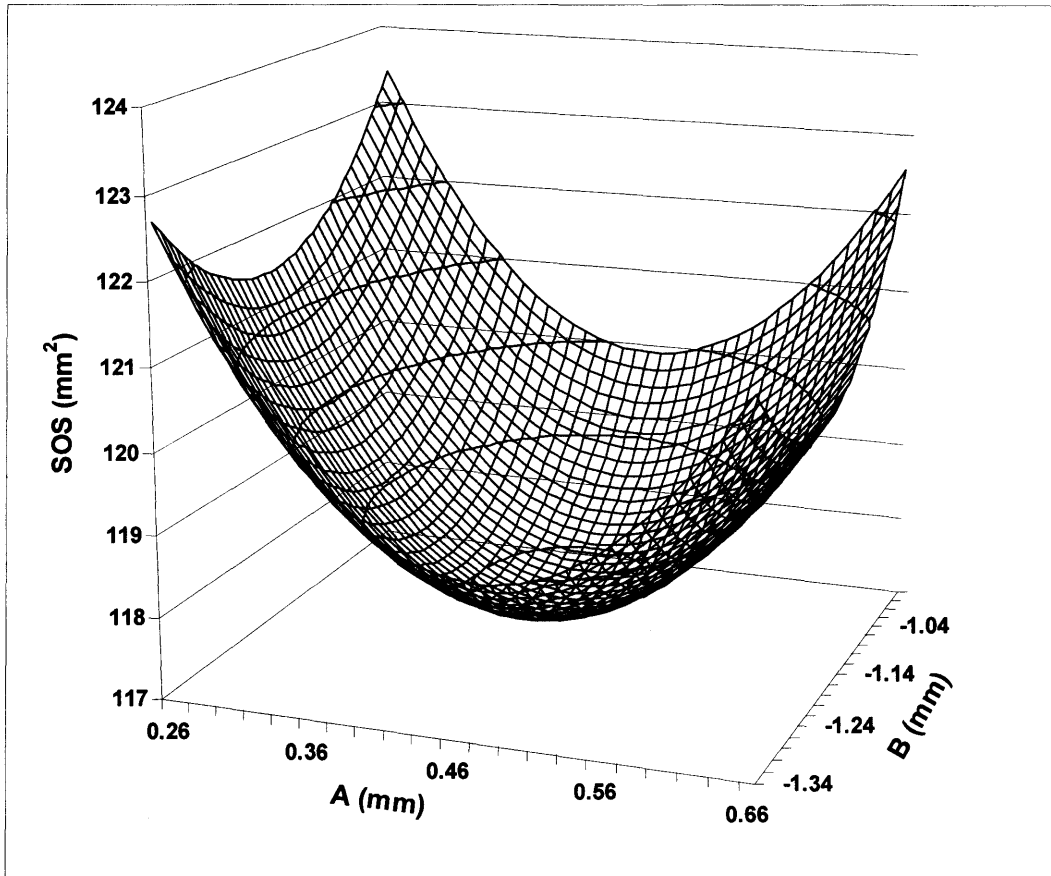


Figure 3-10: Sum of squares (SOS) values of the considered coordinates of the TEPC center (A, B).

The TEPC center coordinate where the SOS value was the smallest, denoting the best fit to the events, was (0.48 mm, -1.18 mm). Using this coordinate as the center of the TEPC, all of the corrected PSD coordinates were shifted so that the TEPC center corresponded to coordinate (0, 0).

With the origin of the coordinate system set to the center of the TEPC, the impact parameter (IP) of each event was calculated with Equation 3-6,

$$IP = \sqrt{X_s^2 + Y_s^2}$$

Equation 3-6

where X_s & Y_s are the corrected PSD coordinates of the event, after being shifted.

The IP of each iron particle that grazed the wall/active volume boundary during the measurement without shielding material were analyzed to determine the spatial resolution of the PSDs. Figure 3-11 displays the distribution of IP of these events. The events with impact parameters less than 5 mm are from particles that hit the anode wires in the active volume of the TEPC.

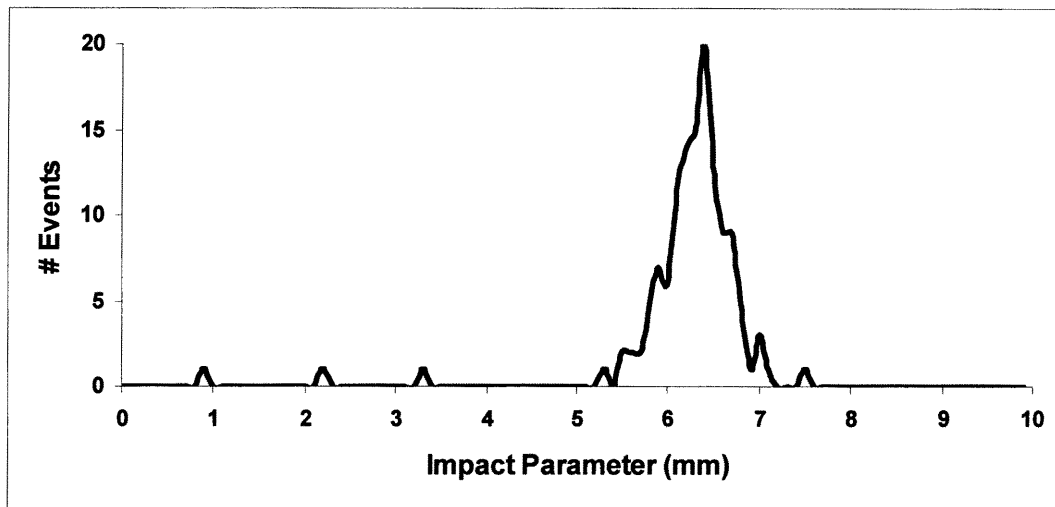


Figure 3-11: Distribution of impact parameters of the events that grazed the boundary of the active volume and the wall during the measurement without shielding material.

The IP distribution was fit to a Gaussian distribution and it had a mean of 6.34 mm and a standard deviation (σ) of 0.34 mm. The full width at half maximum (FWHM) was 0.798 mm (FWHM = 2.355 * σ) and the FWHM/mean was 0.126

(12.6%). The value of the FWHM/mean is a measure of spatial resolution of the PSDs.

Previous experiments, performed by Taddei, exposed an instrument apparatus, similar to the one used in this experiment, to various species of heavy ions. In those experiments, the measured values of FWHW/mean of the PSDs were around ten percent (Taddei 2003). Since the value of FWHM/mean measured in this experiment is similar to the same values measured by Taddei, the spatial resolutions of the PSDs are similar.

Beam Uniformity Correction

The iron beam used in the experiment was not spatially uniform in the plane perpendicular to the beam. In order to obtain spectra of energy deposition in the TEPC (to get TEPC response functions which are used to determine dose equivalent) due to a spatially uniform beam, the events were initially sorted by IP.

For each measurement run with the iron beam, events that hit the TEPC ($IP \leq 8.89$ mm) were sorted by IP. The ranges of IP that the events were sorted into were all initially 1 mm wide (0-1 mm, 1-2 mm, etc.). The reason for sorting the events by impact parameter was due to the spherical symmetry of the TEPC. The selection of 1 mm wide ranges of IP was so that the product of the spatial resolution of the PSDs

(12.6%) and the largest value of IP of an event that hit the TEPC was smaller than any range of IP.

However, the 6-7 mm range of IP contained the TEPC active volume/wall boundary (IP = 6.35 mm). Since the events with IPs less than 6.35 mm pass through the active volume and events with IPs greater than 6.35 mm do not, their patterns of energy deposition in the TEPC are different from one another (as shown in Figure 3-8). To account for these differences, the events that fell into the 6-7 mm range of IP were subdivided into 6-6.35 mm and 6.35-7 mm ranges.

After the events were sorted into ranges of IP, a normalized spectrum of energy deposition in the TEPC was compiled for each range of IP. This was done by first creating a histogram of energy deposition in the TEPC from the events in the range of IP. Then, the histogram was normalized by the number of events in the range of IP. The result was the normalized spectrum of energy deposition for that range of IP.

Next, the normalized spectra of energy deposition in the TEPC for each IP range were individually weighted. The weighting was done by multiplying each spectrum by their respective fraction of the total cross-sectional area of the TEPC. For example, the normalized spectra of energy deposition in the TEPC compiled from events with IPs of 2-3 mm were multiplied by a factor of $\pi * [(3 \text{ mm})^2 - (2 \text{ mm})^2] / [\pi$

* $(8.89 \text{ mm})^2] = 0.0633$. Table 3-1 shows all the IP ranges the events were sorted into and their respective fractions of the total cross-sectional area of the TEPC.

IP Range	Total TEPC Cross-Section Fraction
0-1 mm	0.0127
1-2 mm	0.0380
2-3 mm	0.0633
3-4 mm	0.0886
4-5 mm	0.1139
5-6 mm	0.1392
6-6.35 mm	0.0547
6.35-7 mm	0.1098
7-8 mm	0.1898
8-8.89 mm	0.1902
	$\Sigma = 1$

Table 3-1: Ranges of IP the events were sorted into and their respective fractions of the total cross-sectional area of the TEPC.

After the normalized spectra of energy deposition in the TEPC (from events sorted by IP) were weighted, the spectra from all the ranges of IP were added together. The resultant spectrum was the used as the spectrum of energy deposition in the TEPC from a spatially uniform beam of iron particles.

This process, starting with event sorting and ending with combining of spectra, was performed with the data collected from measurement with and without shielding material in the iron beam.

CHAPTER 4

Results & Discussion

Background & Noise

During each measurement run with the iron beam, a 10 Hz pulser triggered the data acquisition in addition to the coincidence of a signal from the 3 mm Si detector and a signal from the TEPC. In over 99.9% of the events triggered by the pulser, the 3 mm Si detector did not measure an iron particle. Therefore, events triggered by the pulser could be used to measure the response of the TEPC when there were no iron particles traversing the instrumentation apparatus. Figure 4-1 shows the spectra of energy deposition in the TEPC from events triggered by the pulser and from events triggered by 3 mm Si/TEPC coincidence, both obtained from the measurement run with no shielding material in the beam line. Figure 4-2 is the complimentary cumulative distributions of the spectra in Figure 4-1.

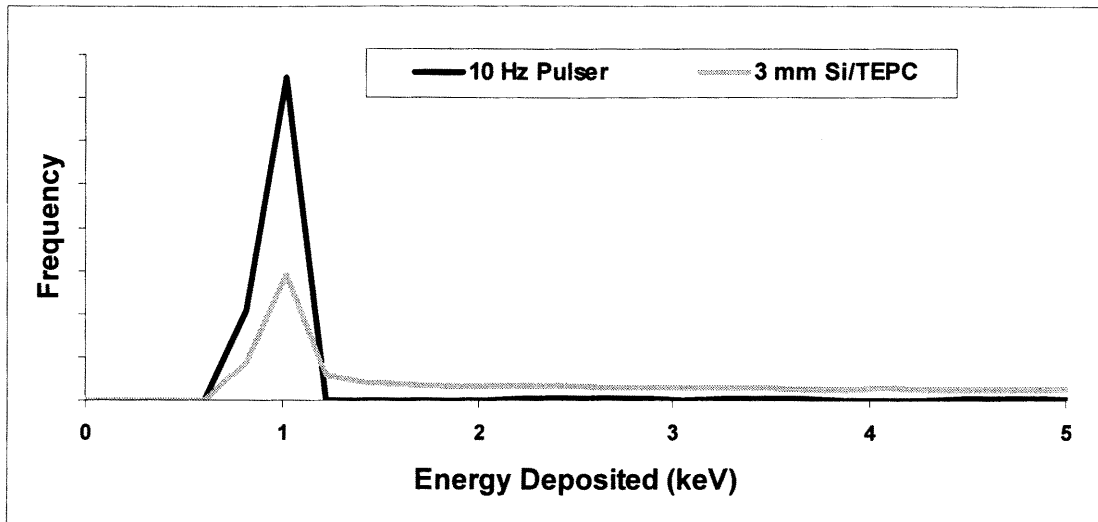


Figure 4-1: Spectra of energy deposition in the TEPC from events triggered by 10 Hz pulser and 3 mm Si/TEPC coincidence during measurement with no shielding material.

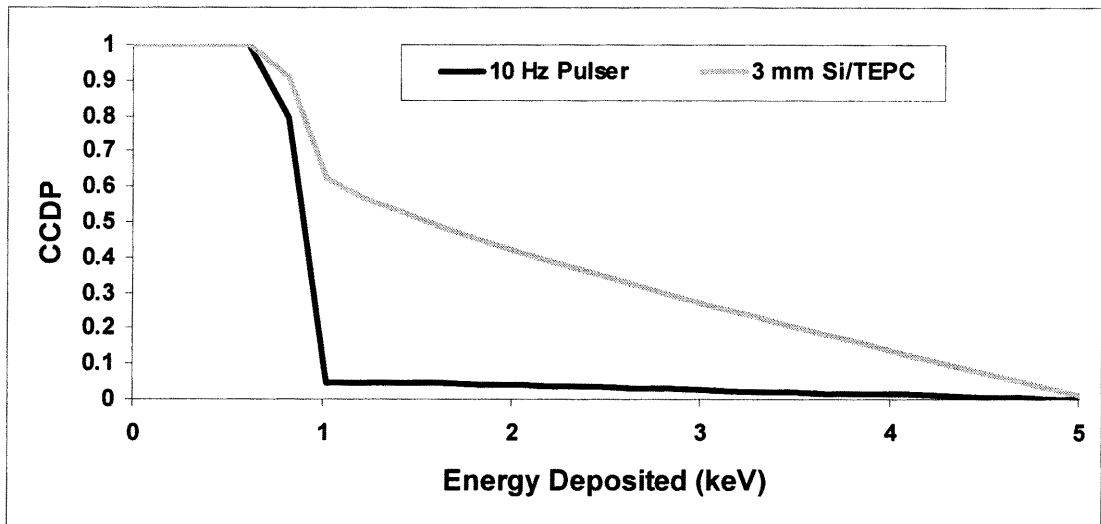


Figure 4-2: Complimentary cumulative distribution probabilities (CCDP) of spectra shown in Figure 4-1.

Both frequency distributions of energy deposition in the TEPC have the same peak at 1 keV. This peak was observed in the measurements with both shielding

materials as well. A reason for the presence of events, triggered by the 3 mm Si/TEPC coincidence, in the peak is the cross-section of the 3mm Si is larger than the cross-section of the TEPC (both in the plane perpendicular to the beam). Therefore an iron particle incident on the 3 mm Si detector may not travel through the TEPC.

The presence of the peak in all the measurement runs indicated that events with energy deposition in the TEPC less than 1 keV were indistinguishable from background radiation and electronic noise and could be discarded. To test this observation, calculations of \bar{y}_F and \bar{y}_D with the data from the unshielded iron beam run were made as a function of threshold or cutoff of energy deposition in the TEPC. Events with energy deposition in the TEPC below the cutoff were not considered in the calculations. Figure 4-3 shows the results of the calculations.

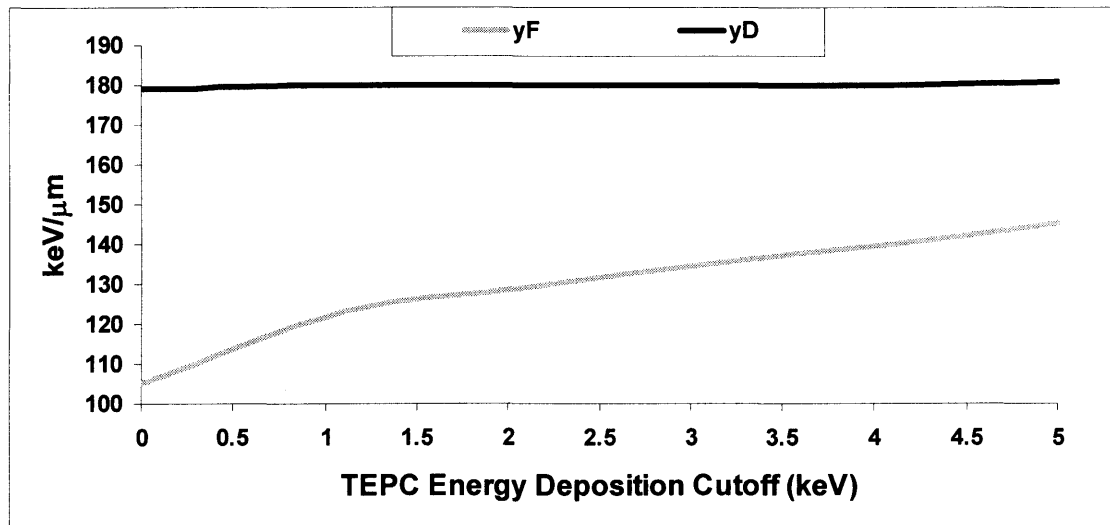


Figure 4-3: Calculations of \bar{y}_F and \bar{y}_D , with data from measurement without shielding material, over changing cutoff of energy deposition in the TEPC.

The value of \bar{y}_D changed insignificantly due to the change in energy deposition in the TEPC cutoff. However, the rate at which the value of \bar{y}_F increases with the raising cutoff lowers at the 1 keV cutoff. This indicates the events with energy deposition in the TEPC up to 1 keV have a pattern different than the events with greater energy deposition. This change in determination of \bar{y}_F , along with the peak in frequency of events at energy deposition of 1 keV in the TEPC from both triggering conditions, gave evidence that most of the events with energy deposition in the TEPC equal to or less than 1 keV were due to background radiation and electronic noise. Therefore these events were not considered in the formulation of the energy deposition in the TEPC spectra and the calculations of \bar{y}_F and \bar{y}_D derived from them.

Uncertainty in Position of Low LET Particles

In addition to the energy deposition in the TEPC, uncertainty can present itself in the positional data of the fragmented iron particles (secondary particles) measured by the PSDs taken during the measurements involving shielding material. Specifically, secondary particles with values of LET less than 10 keV/ μm , produced from fragmentation in the shielding material, do not have their positions accurately measured by the PSDs (Taddei et al. 2006) and thus do not have certainty in whether they traversed the TEPC or not. Therefore a particle with low LET measured by the PSDs as emerging from the TEPC may have actually missed the TEPC altogether.

This phenomenon could lead to events from particles with low LET being used in the formulation of TEPC response functions when they should not.

To determine the contribution to the TEPC response functions from particles of low LET, spectra of energy deposition in the TEPC from the low LET particles were compiled and then the similar spectra from background/noise were subtracted from them. Events from particles with low LET were determined by converting the spectra of energy deposition in the PSDs to spectra of LET. The measurements of energy deposition in the PSDs were calibrated by first locating the peaks in the spectra of energy deposition in the PSDs from unfragmented particles of each measurement. Figure 4-4 displays the spectra of frequency of the energy deposition in the PSDs of each measurement with the beam of iron particles. The channel # of each peak was found and assigned with their corresponding value of LET of unfragmented iron. The LET of the unfragmented iron emerging from the shielding material were calculated with Equation 2-3. Table 4-1 shows the calculated LET of unfragmented iron particles passing through the various shielding materials and their corresponding channel # of the peak in frequency of energy deposition in the PSD.

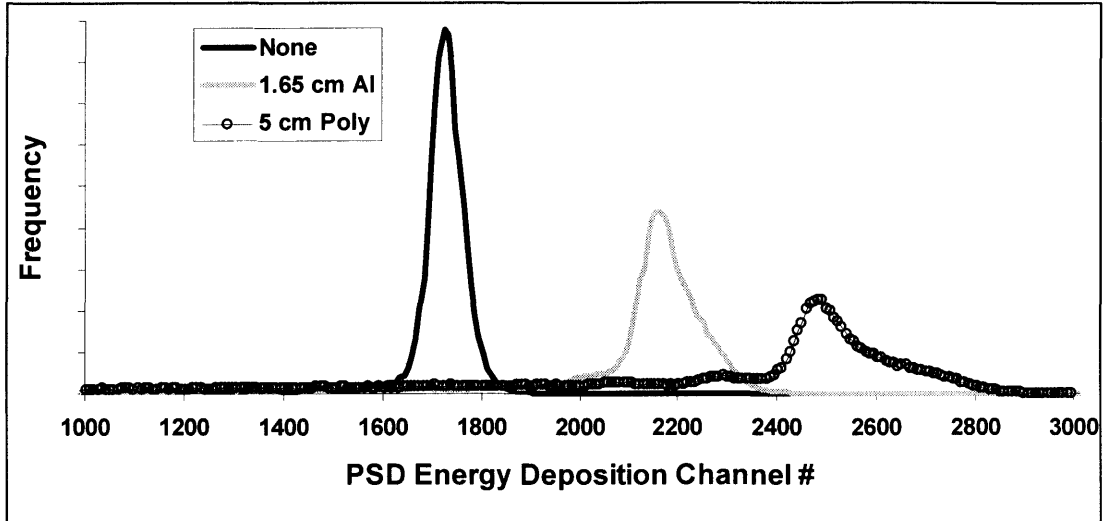


Figure 4-4: Spectra of energy deposition in PSDs during measurements with various shielding materials in the iron beamline.

Shielding Material	LET (keV/ μm)	PSD Energy Deposition Peak Channel #
None	190	1718
1.65 cm Al	220	2165
5 cm Polyethylene	243	2489

Table 4-1: Calculated LET and channel # of the peak of energy deposition in the PSDs from unfragmented iron particles during measurements with shielding material in the beam.

Also, the value of zero LET was correlated to PSD energy deposition channel # zero. Using this and the data in Table 4-1, a linear calibration of the energy deposition in the PSDs to particle LET was created. Figure 4-5 shows a plot of the calibration and the points used to construct it.

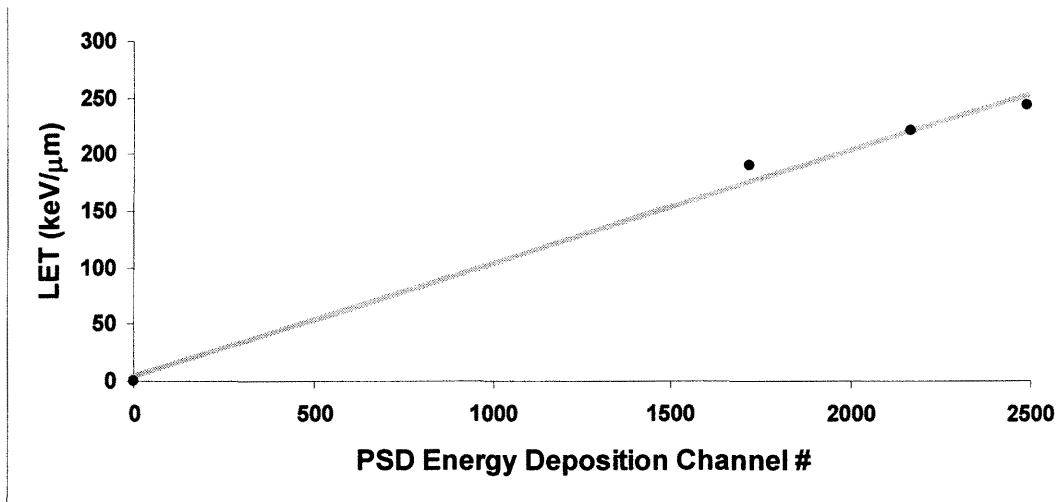


Figure 4-5: Linear calibration of energy deposition in PSD to particle LET.

This calibration was used to determine which channel # of energy deposited in the PSDs correlated to a particle LET of 10 keV/μm. Events at or below this channel #, in the data from the measurement runs with Al and polyethylene in the beamline, were selected as the particles with $LET \leq 10 \text{ keV}/\mu\text{m}$. Table 4-2 displays the percentage of events from particles with $LET \leq 10 \text{ keV}/\mu\text{m}$ for each run with shielding in the iron beam.

Shielding	% events with $LET \leq 10 \text{ keV}/\mu\text{m}$
Aluminum, 1.65 cm	5.8
Polyethylene, 5 cm	5.0

Table 4-2: Percentage of events from particles with $LET \leq 10 \text{ keV}/\mu\text{m}$ measured during the runs with shielding.

These events were used to compile spectra of energy deposition in the TEPC. Additionally, spectra of energy deposition in the TEPC from events triggered by the

10 Hz pulser (background/noise) were compiled from the measurements with shielding material. The spectra from particles with $LET \leq 10 \text{ keV}/\mu\text{m}$ and the spectra from background/noise were then normalized by the number of events used in their compilation.

Next, the normalized spectra compiled from particles with $LET \leq 10 \text{ keV}/\mu\text{m}$ were scaled up such that the values of frequency at 2 keV energy deposited in the TEPC was the same as the value of frequency at 2 keV energy deposited in the TEPC in the normalized spectra compiled from background/noise. The scaled-up spectra was subtracted by the normalized spectra compiled from background/noise. The resultant spectra were normalized by frequency and then used as the spectra of energy deposition in the TEPC from particles with $LET \leq 10 \text{ keV}/\mu\text{m}$. Figure 4-6 shows this subtraction with the data from the measurement with 5 cm polyethylene in the beamline.

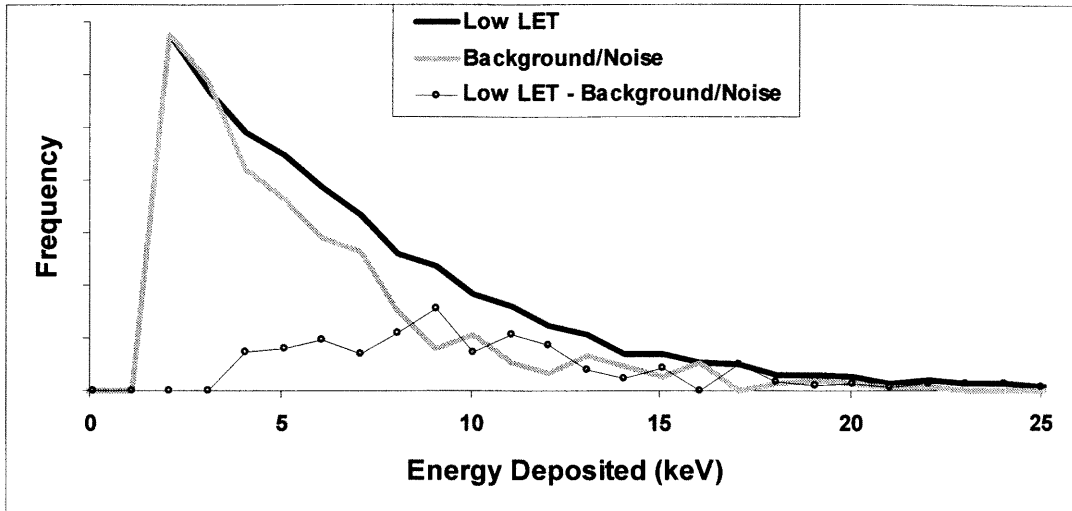


Figure 4-6: Spectra of energy deposition in the TEPC from particles with low LET and background/noise along with the spectrum of their subtraction, during measurement run with 5 cm polyethylene in the beamline.

The objectives of this process was to subtract the spectra of energy deposition in the TEPC, compiled from background/noise, from the similar spectra compiled from the particles with $LET \leq 10 \text{ keV}/\mu\text{m}$ and use the resultant spectra as the contribution to the TEPC response function of particles with $LET \leq 10 \text{ keV}/\mu\text{m}$. How the resultant spectra were incorporated into the TEPC response functions is addressed in the next section.

TEPC Response Functions

The TEPC response functions (spectra of lineal energy in the TEPC) were compiled from measurements taken with 1.65 cm Al, 5 cm polyethylene, and no shielding material in the iron beam. These response functions were determined for two conditions: all particles emerging from the shielding material (primary and

secondary particles) and only unfragmented iron emerging from the beam (primary particles). The compilations took into account the lack of uniformity of the beam.

In the cases of measuring the response of the TEPC to all particles with Al and polyethylene in the beamline, the spectra of energy deposition from particles with $LET \leq 10 \text{ keV}/\mu\text{m}$ were folded into the similar spectra from the other particles, corrected for spatial uniformity of the beam. This was done by multiplying each spectrum by the number of events used in their compilation, adding them together, and then dividing the resultant spectra by the total number of events. The end results were the TEPC response functions from all particles emerging from the Al and polyethylene.

The TEPC response functions to all particles during the runs with 5 cm polyethylene, 1.65 cm Al, and no shielding in the iron beamline are shown in Figure 4-7. Similarly, the TEPC response functions to just unfragmented iron particles (determined by examining the energy deposition in the PSDs) during the measurements with 5 cm polyethylene, 1.65 cm Al, and no shielding in the iron beamline are shown in Figure 4-8.

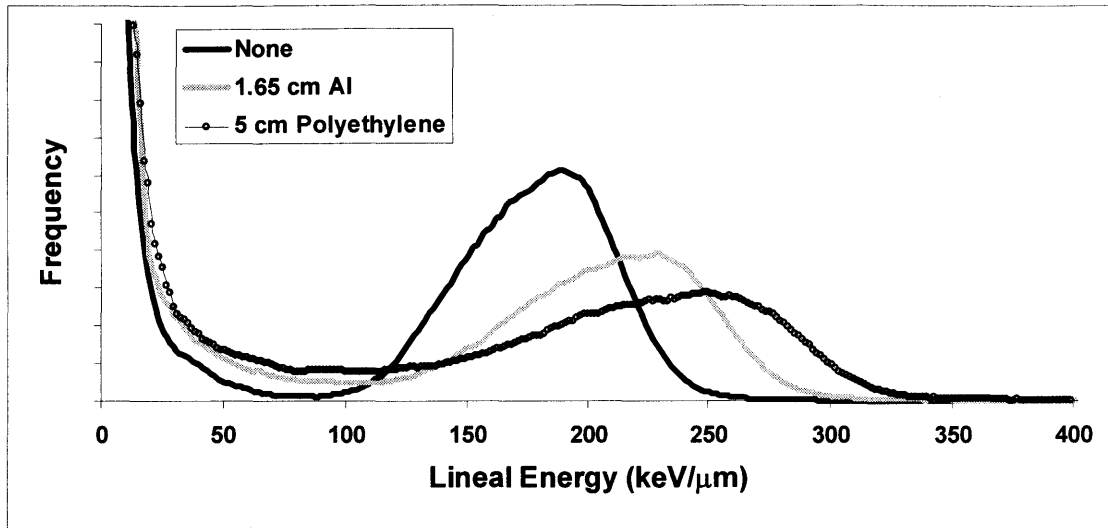


Figure 4-7: TEPC response functions for all particles emerging from various shielding materials when exposed to iron particles at 500 MeV/nucleon.

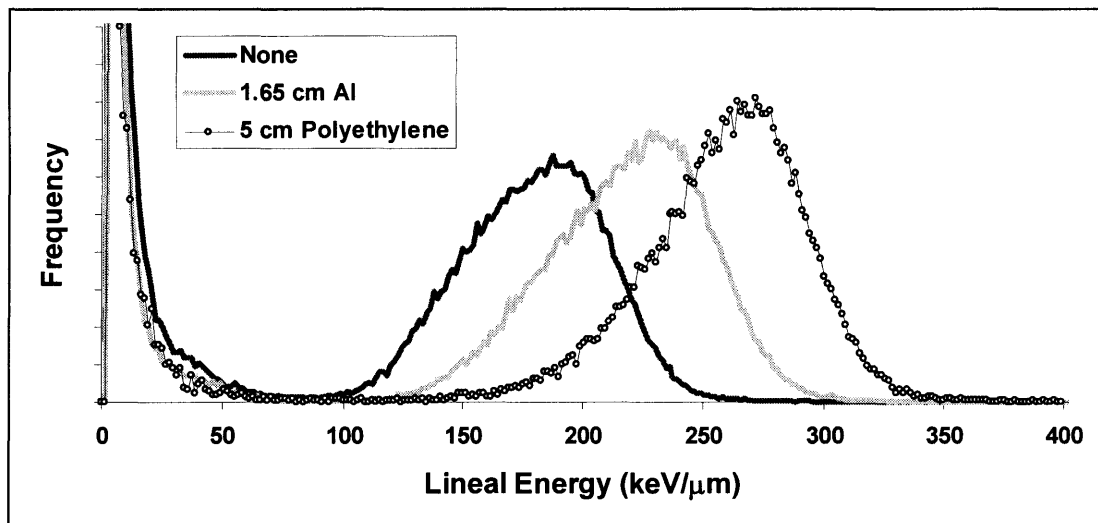


Figure 4-8: TEPC response functions to unfragmented iron particles emerging from various shielding materials when exposed to iron particles at 500 MeV/nucleon.

The TEPC response functions each have two peaks in frequency, one at low lineal energies ($\gamma < 50 \text{ keV } \mu\text{m}^{-1}$) and the other in the 100-325 $\text{keV}/\mu\text{m}$ lineal energy

span. Figure 4-9 displays the TEPC response function with no shielding material in the beamline, from all particles, and highlights the two peaks.

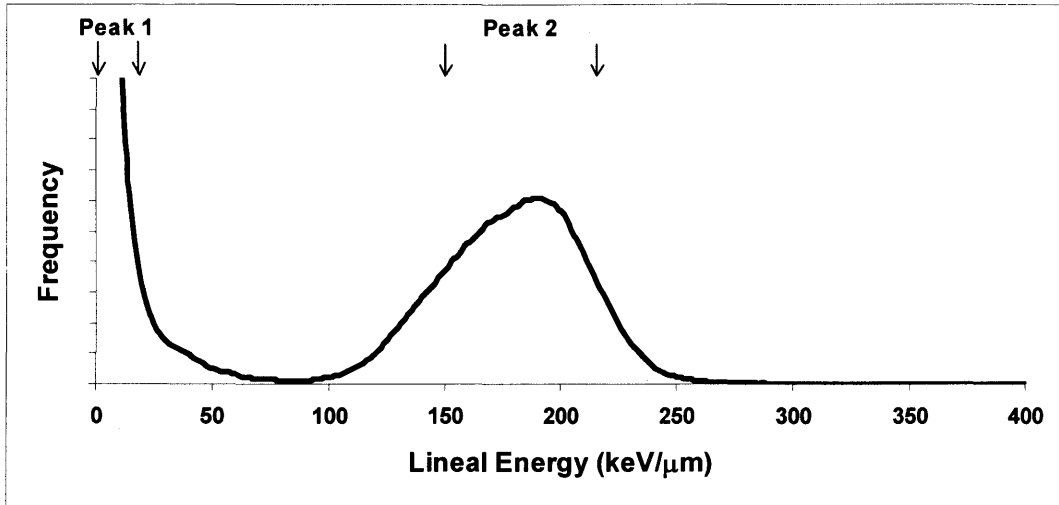


Figure 4-9: TEPC response function from all particles during iron particle irradiation (no shielding material) with the two peaks labeled.

The peak at low lineal energy in the spectrum (Peak 1) is primarily from events that pass through the wall of the TEPC ($IP > 6.35$ mm), as shown in the PSD positional data measured by the PSDs of Figure 4-10.

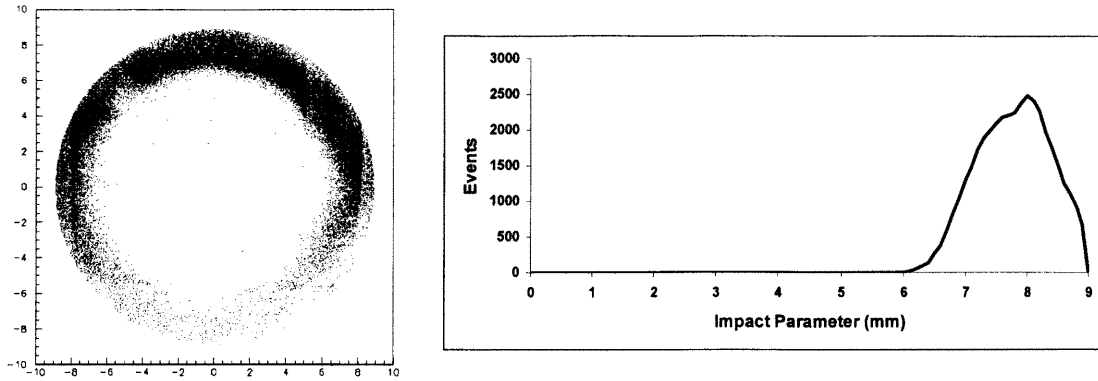


Figure 4-10: Coordinates of events, during measurement with no shielding material, in the first peak ($y \leq 50 \text{ keV}/\mu\text{m}$) of the TEPC response function as measured by the PSDs and their distribution of impact parameters.

Peak 2 in Figure 4-9 is primarily due to particles traveling through the active volume of the TEPC and is centered around $180 \text{ keV}/\mu\text{m}$ lineal energy. Figure 4-11 displays the PSD positional data of the events in the peak and shows that the vast majority of these events passed through the active volume of the TEPC (IP < 6.35 mm).

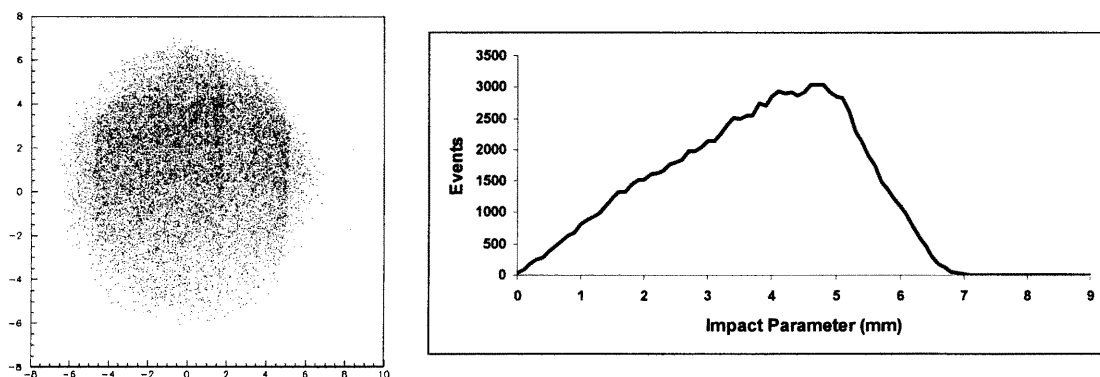


Figure 4-11: Coordinates of events, during the measurement with no shielding material, in the second peak ($100 \leq y \leq 250 \text{ keV}/\mu\text{m}$) of the TEPC response function as measured by the PSDs and their distribution of impact parameters.

The relatively small # of events seen in the lower portion of the fitted PSD positional coordinates of Figures 4-10 and 4-11 is due to the lack of spatial uniformity of the iron beam.

Calculation of \bar{y}_F and \bar{y}_D

The TEPC response functions displayed in Figures 4-7 and 4-8 were used to calculate the value of \bar{y}_F and \bar{y}_D . The results are summarized in Table 4-3 and Figures 4-12 and 4-13.

Shielding	Particles Emerging From Shielding	LET (keV/μm)	\bar{y}_F (keV/μm)	\bar{y}_D (keV/μm)
None	Unfragmented Iron Only	190	123	180
None	All	-	120	179
1.65 cm Al	Unfragmented Iron Only	220	172	221
1.65 cm Al	All	-	119	206
5 cm Polyethylene	Unfragmented Iron Only	243	210	261
5 cm Polyethylene	All	-	124	221

Table 4-3: Calculations of \bar{y}_F and \bar{y}_D from measurements of all particles and only unfragmented iron emerging from various shielding materials irradiated with iron particles at 500 MeV/nucleon along with the calculated values of LET of unfragmented iron particles.

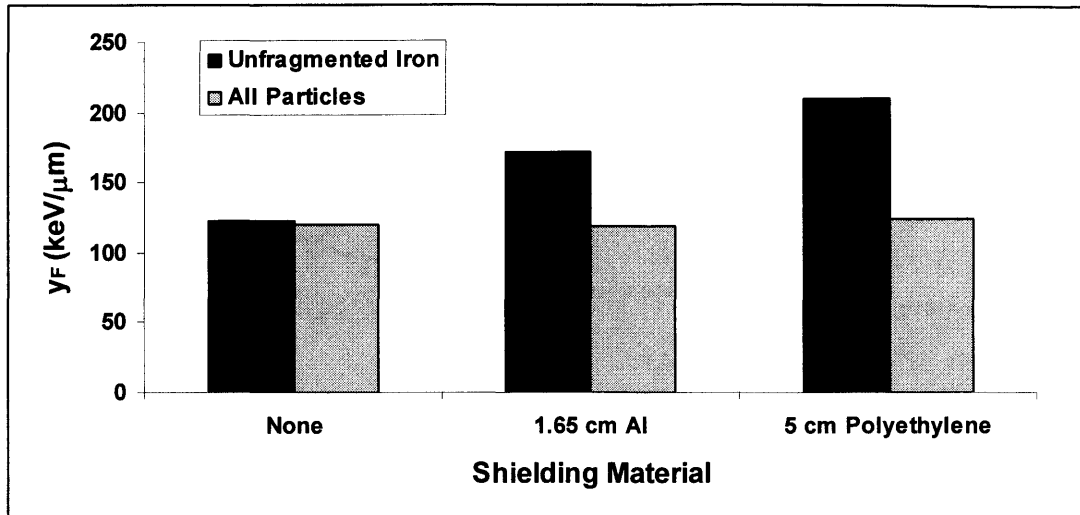


Figure 4-12: Calculations of \bar{y}_F from measurements with various shielding materials in the beamline.

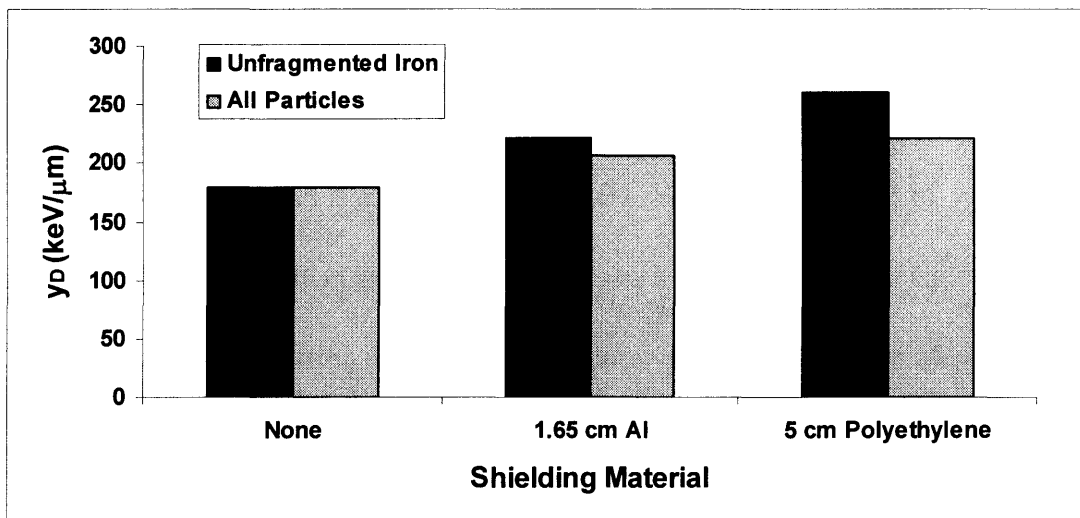


Figure 4-13: Calculations of \bar{y}_D from measurements with various shielding materials in the beamline.

Figure 4-14 shows the values of \bar{y}_F and \bar{y}_D calculated from the exposures of TEPC to the various energies of iron particles (and their LET) performed in this experiment and the experiment performed by Gersey et al. (Gersey et al. 2002).

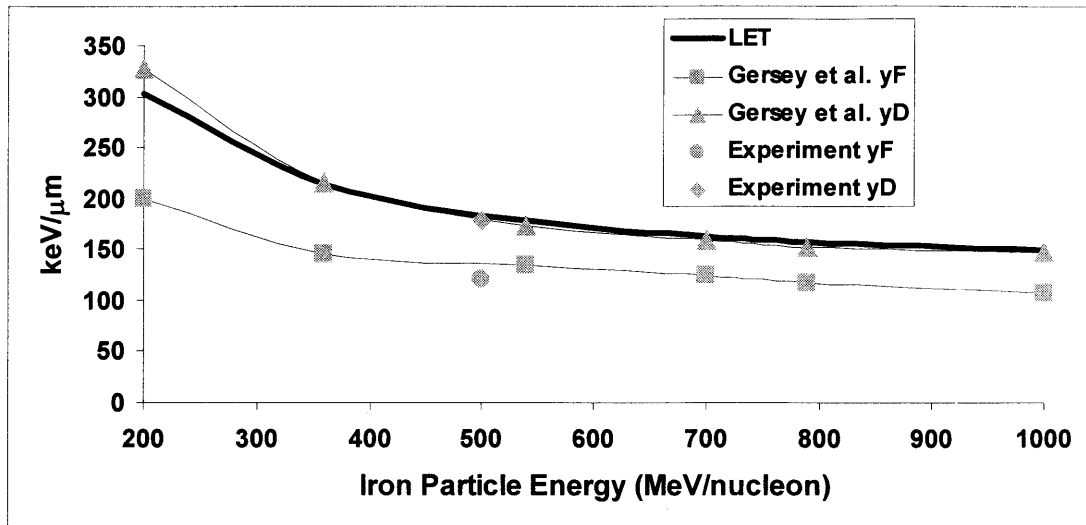


Figure 4-14: Values of \bar{y}_F , \bar{y}_D , and linear energy transfer (LET) of iron particles at various energies in this experiment and the experiment performed by Gersey et al. (Gersey et al. 2002)

The value of \bar{y}_D calculated in this experiment is consistent with the values in the other experiment and is equivalent to the LET. However, the value of \bar{y}_F from this experiment is less than the pattern of \bar{y}_F values found in the other experiment. The difference may be from the instrument apparatus used in the experiments. The apparatus used in the experiment performed by Gersey et al. was similar to the one used in this experiment except there was a pair of PSDs upstream of the TEPC as well as downstream. With the two PSD pairs, they were able to determine the path of each particle through the TEPC (Gersey et al. 2002). This allowed for greater accuracy in determination of the impact parameter of each event they measured with the iron beam.

The measurements of all particles emerging from the shielding resulted in the calculated values of \bar{y}_F not changing when the iron beam was shielded with any of the two materials used in this experiment. Since the value of \bar{y}_F did not change when measuring all particles and it is proportional to absorbed dose, as shown in Equation 2-10, the presence of shielding material did not change the absorbed dose per particle.

However, the increase in the value of \bar{y}_D , when comparing the measurements with shielding material to the measurement without it, indicates that the presence of shielding material increases the average LET of the radiation. As shown in Table 2-2, radiation with an average LET greater than 100 keV/ μm decreases in the quality factor when the average LET increases. Since the presence of shielding material decreases the quality factor while keeping the absorbed dose constant when exposed to iron particles at 500 MeV/nucleon, the dose equivalent from the radiation decreases, providing biologically significant protection.

Furthermore, comparing the values of \bar{y}_D measured with the 1.65 cm Al and 5 cm polyethylene (both with 4.5 g/cm² density thickness) in the beamline show that the polyethylene reduced the average quality of the radiation more than the same density thickness of aluminum. This is consistent with observations made by Wilson et al. that shielding of HZE particles improves as the atomic number of the shielding material decreases (Wilson et al. 1995). Therefore, polyethylene was better at reducing the dose equivalent from 500 MeV/nucleon iron particles when compared to the same density thickness of aluminum.

Considerations for Future Work

In order to further examine the shielding effects of shielding material on HZE particles found in space, additional measurements should be made with additional HZE particle species and energies. The species of HZE particles used should be the elements with significant relative absorbed doses, as shown in Figure 2-1. The LET of the particles examined should be 10-100 keV/ μm and greater than 100 keV/ μm . This would allow for the examination of how the quality factor would change on both sides of the peak in quality factor over particle LET, as shown in Table 2-2. Additionally, measurements should be made with differing thicknesses of the same shielding material. Changing thicknesses of the same type of shielding material would allow for analyses to determine the optimum amount of the shielding material for HZE particles.

CHAPTER 5

Conclusion

An experiment was designed to measure the effects of shielding a beam of iron particles at 500 MeV/nucleon, a dosimetrically-significant species of particles found in space, with a microdosimeter. The shielding material used, in separate measurements, was 1.65 cm aluminum and 5 cm polyethylene (both 4.5 g cm⁻² density thickness). The microdosimeter used was a tissue equivalent proportional counter (TEPC) that simulated 1- μ m size tissue and was apart of a particle spectrometer that measured the linear energy transfer (LET) and position of particles emerging from the shielding material. The experiment was performed at the Heavy Ion Medical Accelerator at the National Institute for Radiological Sciences in Chiba, Japan.

The iron beam used was not spatially uniform. Analysis was done offline to produce TEPC response functions from a uniform beam. Low LET particles, produced from the fragmentation of iron particles in the shielding material, did not have their positions measured accurately. Offline analysis was done to account for the uncertainty. The analyses produced TEPC response functions for all particles and for just unfragmented iron emerging from each shielding material.

The TEPC response functions were used to calculate the frequency mean lineal energy, \bar{y}_F , and dose mean lineal energy, \bar{y}_D , of each shielding scenario. The value of \bar{y}_F can be used to calculate the absorbed dose per particle and the value of \bar{y}_D can be used to approximate the average LET of the radiation, which is used to determine the average quality factor of the radiation. The calculations of \bar{y}_F and \bar{y}_D showed that the Al and polyethylene shielding reduced the quality factor of the iron particles, but had no effect on the absorbed dose per particle. The polyethylene was found to be better at reducing the quality factor than aluminum at the same density thickness. Future work should be done to measure the effects of shielding the other dosimetrically-significant species of particles found in space, at various values of LET, and with varying thicknesses of shielding.

REFERENCES

Badhwar,G.D., Konradi, A. Hardy,A., Braby, L.A., Active Dosimetric Measurements On Shuttle Flights. Nucl. Tracks Radiat. Meas. 20, 13-20 1992.

Badhwar,G.D., Cucinotta, F.A. A Comparison of Depth Dependence of Dose and Linear Energy Transfer Spectra in Aluminum and Polyethylene. Radiat Res. 153, 1-8 2000.

Gersey, B., The Response of a Spherical Tissue-Equivalent Proportional Counter to Iron Particles from 200-1000 MeV/nucleon, Ph.D. thesis, Colorado State University, Fort Collins, 2006.

Gersey, B., Borak, T., Guetersloh, S., Zeitlin, C., Miller, J., Heilbronn, L., Murakami, T., Iwata, Y., The Response of a Spherical Tissue-Equivalent Proportional Counter to ⁵⁶Fe Particles from 200-1000 MeV/nucleon. Radiat Res. 157, 350-360, 2002.

Guetersloh, S.B., Borak, T.B., Taddei, P.J., Zeitlin, C., Heilbronn, L., Miller, J., Murakami, T., Iwata, Y., The Response of a Spherical Tissue-Equivalent Proportional Counter to Different Ions Having Similar Linear Energy Transfer. Radiat. Res. 157, 350-360, 2002.

International Commission on Radiation Protection, Annals of the ICRP: 1990 Recommendations of the International Commission on Radiological Protection, International Commission on Radiation Protection, New York, 1991.

International Commission on Radiation Units and Measurements, ICRU Report 36, Microdosimetry, International Commission on Radiation Units and Measurements, Maryland, 1983.

Kellerer, A. M., Rossi, H. H., "Summary of Quantities and Functions Employed in Microdosimetry," In *Second Symposium on Microdosimetry* (Ebert, H. G., Ed), pp. 843-853, Commission on the European Communities, Brussels, Belgium, 1968.

Knoll, G. F., "Radiation Detection and Measurement", John Wiley & Sons, New York 2000.

NCRP, Guidance on Radiation Received in Space Activities. Report 98, National Council on Radiation Protection and Measurements, Bethesda, MD, 1989.

NCRP, Ionizing Radiation Exposure of the Population of the United States. Report 93, National Council on Radiation Protection and Measurements, Bethesda, MD, 1987.

NCRP, Radiation Protection Guidance for Activities in Low Earth Orbit. Report 132, National Council on Radiation Protection and Measurements, Bethesda, MD, 2000.

NIRS, Heavy Ion Medical Accelerator in Chiba – A Design Summary and Update, National Institute of Radiological Sciences, Chiba, Japan, 1992.

Rademacher, S.E., Borak, T.B., Zeitlin, C., Heilbronn, L., Miller, J., Wall Effects Observed in Tissue-Equivalent Proportional Counters from 1.05 GeV/nucleon Iron-56 Particles. *Radiat Res.* 149, 387-395 1998.

Simpson, J.A., Elemental and Isotopic Composition of Galactic Cosmic Rays. *Annu. Rev. Nucl. Part. Sci.* 33, 323-382 1983.

Taddei, P.J., The Response of a Spherical Tissue-Equivalent Proportional Counter to Different Heavy Ions with Similar Velocities, Ph.D. thesis, Colorado State University, Fort Collins, 2003.

Taddei, P.J., Borak, T.B., Guetersloh, B.B., Zeitlin, C., Heilbronn, L., Miller, J., Murakami, T., and Iwata, Y. The Response of a Spherical Tissue-Equivalent Proportional Counter to Different Heavy Ions Having Similar Velocities. *Radiat. Meas.* 41, 1227-1234, 2006.

Turner, J.E., "Atoms, Radiation, and Radiation Protection," McGraw-Hill Inc., New York, 1995.

Wilson, J.W., Kim, M., Schimmerling, W., Badavi, F.F., Thibeault, S.A., Cucinotta, F.A., Shinn, J.L., Kiefer, R. Issues in Space Radiation Protection: Galactic Cosmic Rays. *Health Phys.* 68(1), 50-58, 1995.

Wilson, J.W., Cucinotta, F.A., Miller, J., Shinn, J.L., Thibeault, S.A., Singleterry, R.C., Simonsen, L.C., Kim, M.H.Y. Materials for Shielding Astronauts From the Hazards of Space Radiation. *Mat. Res. Soc. Symp. Proc.* 1999: 551;3-15.